ELECTROSTATIC MEMS ACTUATORS FOR ENDOSCOPIC IMAGING AND HIGH RESOLUTION DISPLAYS

by

Sertan Kutal Gökçe

A Thesis Submitted to the
Graduate School of Engineering
in Partial Fulfillment of the Requirements for
the Degree of

Master of Science
in
Electrical and Computer Engineering
Koc University

August 2010

Koc University

Graduate School of Sciences and Engineering

This is to certify that I have examined this copy of a master's thesis by

Sertan Kutal Gökçe

and have found that it is complete and satisfactory in all respects,
and that any and all revisions required by the final
examining committee have been made.

Committee Members:

_____

Hakan Ürey, Ph. D. (Advisor)

_____

Erdem Alaca, Ph. D.

_____

Erdal Bulgan, Ph. D.

Date: _____

ABSTRACT

Laser scanning utilizing MEMS mirrors is used in many display and imaging applications. These systems utilize mirrors to steer the beam and thus require beam folding. There are applications, such as the forward-looking endoscopic imaging probe, where the system needs to fit in a tiny tube. Beam steering with cascaded MLA (Micro Lens Array)s require only small lateral displacements to achieve high angular beam steering. In that sense, beam steering with MLAs integrated MEMS propose a new solution to a forward-looking endoscopic imaging probe.

In the first main part of this thesis, a novel 2 degree-of-freedom(DOF) MEMS stage with one uniaxial set of comb fingers is presented. Mechanical design progress, microfabrication results and characterization of both only 2D MEMS stages and MLA integrated 2D MEMS stages are presented in the first part of thesis. With 1.1mm x1.1mm MLA integrated device, 124 μm out-of-plane deflection is achieved with an applied voltage of 100 Volt in resonance frequency and 34 μm in-plane deflection is achieved with an applied voltage of 57 Volt again in resonance frequency.

In the second main part of the thesis, a novel comb actuated torsional MEMS scanner utilizing indirect drive method is presented. Electrostatic MEMS scanners meet the requirements of high frequency scan speed, large scan angle, and low power consumption. With an applied voltage of 298 Volt, 26.7º Total Optical Scan Angle (TOSA) is obtained at resonance in ambient conditions, where in vacuum TOSA of 36.18º is achieved with an applied voltage of 113 Volt again in resonance.

Keywords: MEMS, Electrostatic Scanners, Comb Actuators

ÖZET

MEMS aynalar kullanarak lazer taraması birçok görüntüleme ve ekran sistemlerinde kullanılmaktadır. Bu tip sistemler ışığı yönlendirmek için ayna kullanırlar ve bu sebepten ışığın belirli bir alan içerisinde yönlendirilmesini gerektirir. Bazı uygulamalar, örnek olarak doğrusal bakan endoskopik görüntüleme uçları, hacimsel olarak küçültme gereksinimi içerisindedir. Mikro Lens Dizinleri (MLD) ile yüksek çözünürlüklü görüntüleme mümkündür, ve çok küçük yerdeğiştirme hareketi ile çok büyük açısal tarama gerçekleştirilebilinir. Klinik ortamlarda, küçük ve geliştirilmiş görüntüleme sistemlerine ihtiyaç vardır. MLD ile entegre edilmiş MEMS aygıtları bu gereksinimleri karşılayark yüksek çözünürlüklü küçültülmüş görüntüleme sistemleri için bir seçenek sunmaktadır.

Tezin ilk kısmında, yeni bir tek elektrostatik parmak takımıyla 2 boyutta tahriklenen MEMS aygıtı sunulmuştur. MEMS aygıtlarıyla entegre tarama sisteminin gerçekleşmesi için polimer MLDler aygıtların üzerine fabrikasyon sonrasında yerleştirilmiştir. Bu tezde 2 boyutlu MEMS aygıtlarının mekanik tasarım süreci, mikrofabrikasyon sonuçları , deneysel sonuçları sunulmuştur. MLD entegre edilmiş MEMS tahrikleyiciler ile 100 Volt uygulanarak 124 μm düzlem dışı hareket elde edilmiştir. Düzlem içi kayma modunda ise 34 μm hareket 57 Volt gerilim ile elde edilmiştir.

Tezin ikinci kısmında, elektrostatik parmaklarla tahriklenen ve dolaylı şekilde sürülen yeni bir MEMS tarayıcı sunulmuştur. Elektrostatik parmaklarla tahriklenen MEMS tarayıcılar az güç harcama, geniş açı taraması, yüksek frekans tarama özellikleri gibi görüntüleme sistemlerinde kritik olan gereksinimleri karşılayabilmektedir. Bu tezde anlatılan MEMS tarayıcı tek çerçeve tarayıcılardan farklı olarak çoklu çerçeveden oluşmuştur. 298 Volt gerilimle havada 26.7 derece optik tarama ve vakumda ise 113 Volt ile 36.18 derece optik tarama elde edilmiştir.

Anahtar Sözcükler: MEMS, Elektrostatik Tarayıcılar, Parmak Tahrikleyiciler

To my orange blossom scented beautiful hometown Adana…

Benim portakal çiçeği kokan güzel şehrim Adana'ya...

ACKNOWLEDGEMENTS

I would like to express my gratitude to my M.Sc. thesis advisor, Professor Hakan Ürey, for the support and guidance he provided me throughout my study. I would like to declare that I was privileged to work with him.

I would like to declare my gratitude to Professor Erdal Bulgan and Professor Erdem Alaca for their contributions to my thesis and accepting to be in the thesis committee.

I acknowledge TUBITAK (Scientific and Technological Research Council of Turkey) for providing the financial support during my master studies and KOC University for the scholarship and providing a great research environment during my master studies. I gratefully acknowledge my undergraduate university METU (Middle East Technical University) for providing great academic and social environment.

I am grateful to Professor Gönül Turhan Sayan and Professor Barış Taşkın, they have always supported my ambition of pursuing an academic career. They always shared their ideas and advices. I am really grateful to their helps.

I would like to declare my thanks to Professor Yusuf Leblebici for his help during our times that we spent in EPFL. I am thankful to Professor Demircan Canadinç for his helps during mechanical design of the actuators and his great course, from which I got new ideas and have learnt many new aspects of engineering applications.

I would like to thank all past and present OML members, without them, this work would not be possible. I owe special thanks to Sven TS Holmström for the great intellectual conversations, and his great friendship. I would like to thank Onur Ferhanoğlu and Erdem Erden for his endless encouragement, motivation, and his great friendship. Special thanks to Selim Ölçer, for his magical hands, marvelous skills, without them this MLA mounting stuff would not go beyond a dream. Special thanks to Gökhan Hatipoğlu, R.Burak Erarslan, N.Pelin Ayerden, Hüseyin Rahmi Seren, Aslıhan Arslan,Duygu Kutluoğlu for their good and sincere friendship and for all funny times that we had with. I

would like to thank also Çağlar Ataman and Fatih Toy for sharing their knowledge and experience when I needed.

I would like to thank Dean Brown, Wyatt O. Davis, Mark Helsel and David Bowman for their great contributions to my knowledge and experience in MEMS design. MEMS stage fabrication was impossible without the efforts of CMI people: Philippe Flückiger, Cyrille Hibert, JB Bureau, Boris Lunardi, Nareg Simonian, Guy F.Clerc, George A. Racine, Claudia D'Agostino.

Thanks to Fahrettin Fırat Gönen: He was always patient and helpful during the experiments and was a good friend all the time. I thank Utku Baran , he was always a good friend and also a good teammate during telecons. I had great time with my flatmates, and special thanks go to Can Yağlı, Emre Yüce, Yunus Emre Has, Yasin Yılmaz. We were always like a team in Kiptaş.

I would like to express my gratitude to my old friends, Denizcan Soner, Umut Toklu, Emre Aytekin, Murat Atak, Önder Uçar, Sabit Sağır, Utku Özkan, maybe we were not always together but I always knew that they were with me when I needed.

My time spent at Koç was made special through social interactions with these friends: Meriç Ataman, İbrahim Gür, E. Pinar Karabulut, Emre Bıyıklı, Övünç Demir, Burçin Onay Deniz Erbulut, Onur Öztaş. I would like to thank all my friends in Lausanne, with whom I shared great time: S.Zeynep Temel, Anıl Yüce, Onur Kazanç, Ata Tuna Çiftlik, Yüksel Temiz.

Lastly but not at least, I declare my deepest and immense gratitude to my family for always making me feel privileged and never putting boundaries to my dreams.

TABLE OF CONTENTS

LIST OF TABLES

LIST OF FIGURES

NOMENCLATURE

MLA	*microlens array*
MMLA	*movable microlens array*
DMLA	*double microlens array*
PSL	*prescan lens*
fPSL	*focal length of the prescan lens*
fMLA	*focal length of the microlens array*
n	*refractive index of the material*
r1	*lateral displacement of the prescan lens*
r2	*lateral displacement of the microlens array*
α	*the beam scan angle constituted by displacements of PSL*
β	*the beam scan angle constituted by displacements of MLA*
θt	*total beam scan angle*
U_E	*the stored energy*
C	*capacitance in charge*
V	*applied voltage difference*
F_X	*electrostatic force along x-axis*
w	*width of comb finger*
g	*the gap between comb fingers*
l	*the length of the comb finger*
lo	*lateral overlap of the comb fingers*
N	*number of the total capacitances*

f_r	*the mechanical resonance frequency of the system*
f_1	*first jump frequency*
f_2	*second jump frequency*
θ_i	*mechanical scan angle of the inner frame*
θ_o	*mechanical scan angle of the outer frame*
ω_{OP}	*the resonance frequency of the out-of-phase torsion mode*
ω_{IP}	*the resonance frequency of the in-phase torsion mode*

Chapter 1

1 Introduction

Miniaturization has become one of the hot engineering topic of interest since the first use of silicon as a mechanical material [1]. Micro-Electro-Mechanical-Systems (MEMS) are compact systems enabling miniaturization of compact macro scale systems into micro scale environment. The applications of MEMS show great diversity including, but not limited to, biological detection systems[2], confocal microscopy[3], microphones [4]. The Micro-Opto-Electro-Mechanical-System (MOEMS) is one of the mainstream application areas of MEMS. As MOEMS goes toward more functional and reliable devices, the motivation for different applications increases as well. Some applications of MOEMS can be classified into telecommunication systems [5], endoscopic systems[6], displays [7]. Some examples of MOEMS for displays and telecommunications are shown in Figure 1.1 and Figure 1.2.

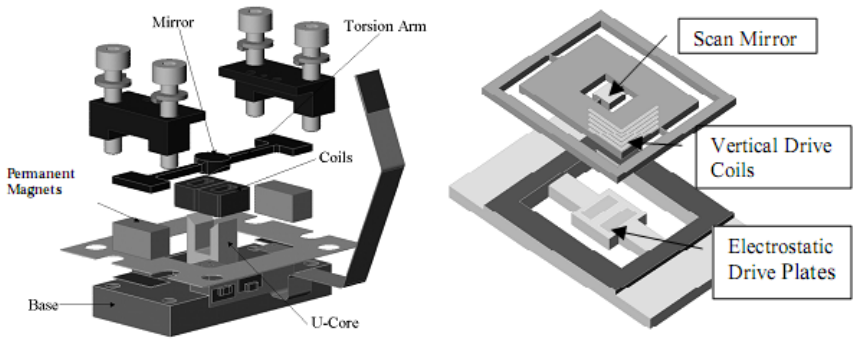

Figure 1.1: Two different microscanners by Microvision: a)Uniaxial Scanner, b)Biaxial MEMS Scanner [7]

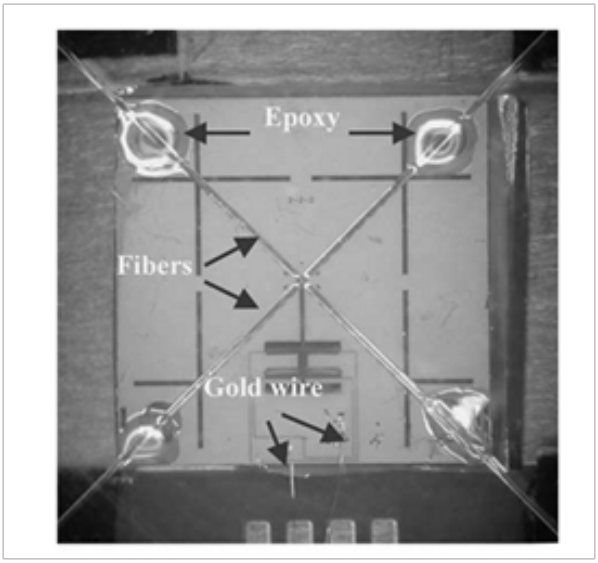

Figure 1.2: Microscopic view of micromachined 2x2 optical switches aligned with fibers [5]

The actuation is one of the main types of uses of MEMS. Transduction between different domains constitutes the main part of actuation in MEMS. There are different actuation mechanisms used in MEMS devices. Some of these mechanisms can be exemplified as follows electromagnetic [8-9], electrostatic [10-11], piezoelectric [12-13].Electrostatic actuation is also called capacitive actuation because this type of actuation most commonly uses electrostatic comb fingers or closing gap capacitive structures as the base of actuation. Electrostatic actuation constitutes the most commonly used actuation mechanism among all others, due to its compactness, low power consumption, and fairly simpler microfabrication. The main principle behind electrostatic actuation is the attractive forced created by two charged plates with a separation of dielectric layer lying between plates. The force or torque produced by two charged plates is dependent on the interaction surface area between plates, the potential difference, and dielectric strength of the layer lying between plates.

This study covers the work done on design, micro-fabrication and characterization of electrostatically actuated the 2D MEMS translational stages integrated with MLAs for endoscopic imaging and high frequency torsional microscanners for high resolution dispalys. Chapter 1 introduces different use of MEMS technology for today's popular technology fields. This chapter emphasizes mainly on MEMS applications in display and imaging, biomedical imaging and telecommunication industry. After the introduction of brief background information of use of MEMS technology, the chapter concludes with giving a background on beam steering with cascaded MLAs.

Chapter 2 gives brief theoretical information on electrostatic comb actuators. Different geometries and of comb finger actuators are presented in this chapter, the capacitance extraction for two different type of translation is carried out in ANSYS CMATRIX macro. The capacitance curve for these translations are described.

Chapter 3 gives information on whole progress on 2D MEMS translational stages. In the beginning, the geometry of the device is introduced. Later, FEM analysis for 2D MEMS translational stages without MLA and MLA integrated stages are presented. After that, the microfabrication details of the actuator are discussed and possible improvements for a future fabrication run are given as well. And the chapter is concluded with characterization results of 2D MEMS stages with and without MLA, and moreover beam steering achieved with MLA integrated stage is given in the final part of this chapter.

Chapter 4 presents high frequency torsional scanner, which also employs electrostatic comb fingers for actuation. This scanner utilizes mechanical coupling principle to decrease air damping and the scanner comprises three frames to decrease dynamic deformation by increasing isolation between actuator side of the scanner and the mirror plate. The chapter starts with the introduction of giving details about the geometry of the torsional scanner. After that, FEM analysis for the scanner is given. This part is followed by the microfabrication details of the scanner. After that, the characterization results carried out

both in ambient and vacuum are given. The chapter is concluded with a comparison of the torsional scanner with other scanners presented in the literature.

Last part of the thesis is the conclusions part. The results of these two different electrostatically actuated MEMS devices are given and possible iterations on the design level to enhance these devices are also presented.

1.1 MOEMS Applications for Display and Imaging

1.1.1 Biomedical Imaging

Miniaturization plays an important role for noninvasive imaging tools. In that sense, MEMS have started to take place in biomedical imaging systems. In recent years, the use of MEMS scanners in the field of optical coherence tomography (OCT) and confocal microscopy have been demonstrated in [14-15]. OCT is similar to ultrasound imaging in terms of working principle where OCT provides a better longitudinal resolution. OCT principally uses interferometry to produce a meaningful signal. The reflected light from the sample tissue and the reference beam produces an interference pattern. This interference pattern is detected and converted to a meaningful signal.

Confocal microscopy is a high-resolution 3D imaging tool. Some confocal microscopy approaches in the literature also use MEMS scanners to guide the light into the desired direction. Light emitted from the source is focused on the target sample and reflected light is collected with the aid of a pinhole to eliminate out of focus light. The MEMS scanner scans the target sample in two dimension providing high accuracy and stability.

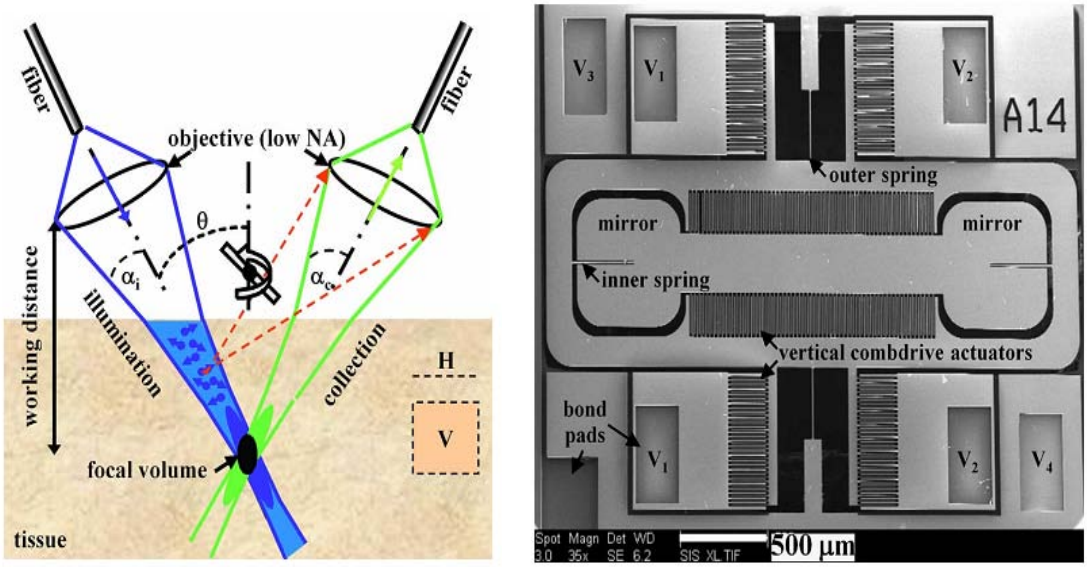

a) **b)**

Figure 1.3: a) Dual–axes confocal microscopy configuration with separate optical fibers b) Scanning Electron Microscope (SEM) image of 2D MEMS scanner for dual axes confocal microscopy [15]

Piyawattanametha et al. showed a dual axes confocal microscopy using MEMS scanners [15] in which they used two optical fibers lying along two different optical axis, see Figure 1.3. As can be seen in Figure 1.3a, in front of each fiber, there is a low numerical aperture (NA) objectives to decrease the sensitivity to off-axis aberrations see. The overlapped region between incident and reflected light defines focal volume. In this work electrostatically actuated 2D MEMS scanners were fabricated for beam scanning, see Figure 1.3b.

Endoscopic laser cameras also utilize MEMS scanners for the sake of miniaturization and the necessity of compactness of the systems. Chong et al. have developed a MOEMS component to be used in fiber optic endoscope eliminating the need for an external power supply [17].In this work two different fiber sources are used; through one of these the modulated optical signal to drive electrostatic MEMS scanner. The proposed scanner achieved a static scan angle of 0.47 with applied 5Vdc.

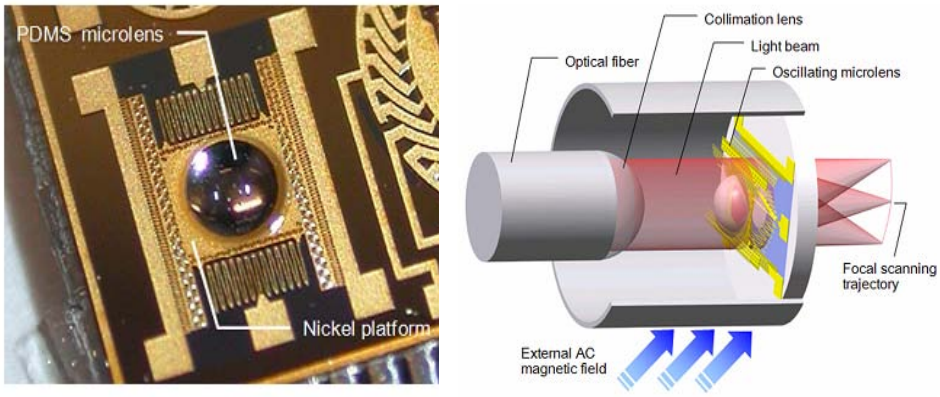

a) b)

Figure 1.4: a) A close-up view of electromagnetic actuator integrated with PDMS microlens b)An exemplary view of a magnetically actuated microlens as a scanning platform[16]

Siu et al. has shown a magnetically actuated MEMS scanner. The scanner is integrated with PDMS microlens for *in vivo* imaging [16].The scanner platform consists of PDMS microlens, ferromagnetic platform, a hinge and suspension springs, see Figure 1.4a. The applied magnetic force on the device creates a periodic focal scanning trajectory. The whole system is compact consisting of an external Alternating Current (AC) magnetic field source, collimating lens, optical fiber and a MEMS scanner. They achieved to have a

scanning pattern of 125.6μm scanning range by applying $22.2x10^{-3}$ Tesla of external magnetic field.

1.1.2 Display and Imaging Systems

Miniaturized display and imaging systems increased the interest in MEMS scanners because MEMS scanners can meet the high resolution, low power consumption, and high scanning speed requirements in miniaturized and imaging systems. In principle, imaging through 2D scanning requires a laser beam, a mechanical scanner unit, and a detector.

Digital display systems constitute the interface for digital video and broadcasting. One of the most successful commercial MEMS products is Digital Micro-mirror Device by Texas Instruments©. DMD is used as a light engine for Digital Light Processing™ Moreover, the DMD based DLP systems have led to different commercial products. They have been serving several markets: large auditorium theaters, home theaters and pocket projectors. DMD is an array of light switches, which are fabricated by CMOS-like process. Each light switch has an aluminum mirror and acts like a digital switch. There are two states of the switches as in almost all digital systems which are illustrated. In (1) state, the mirror switches to +10 degree and when the memory line is in (0) state it switches to -10 degree. Figure 1.5 depicts two DMD mirrors at which one mirror is in (1) state and the other is in (0) state [18].

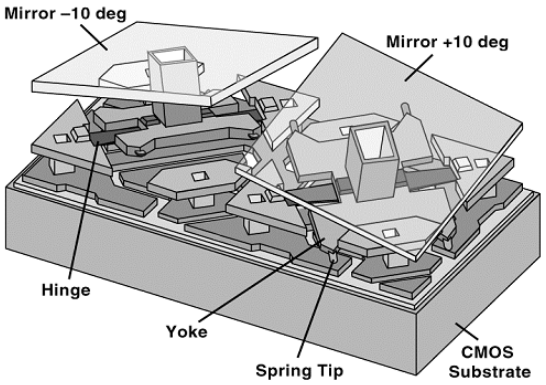

Figure 1.5: The illustration of two states of DMD mirrors

Figure 1.5 shows two different mechanical states used in DMDs , as can be understtod from the figure the MEMS part of the product is fabricated on CMOS (Complementary Metal Oxide Semiconductor) substrate.

Another type of MEMS product used in display systems are single micromirror devices. It can be described as MEMS platforms consisting one suspended movable frame and connected to the substrate via hinges. There will be only brief information given on single micromirror devices here; in Chapter 4 an example of torsional micromirror device is given in detail. Different actuation mechanisms could be utilized for these micromirror devices. Electrothermal actuation is one of these that can be used for mirror scanning. Schweizer et al. developed a 2D bimorph thermally actuated raster scanner,[19]. The raster scanning was achieved one micromirror integrated with L-shaped, thermally actuated bimorph beam as can be seen from Figure 1.6a.

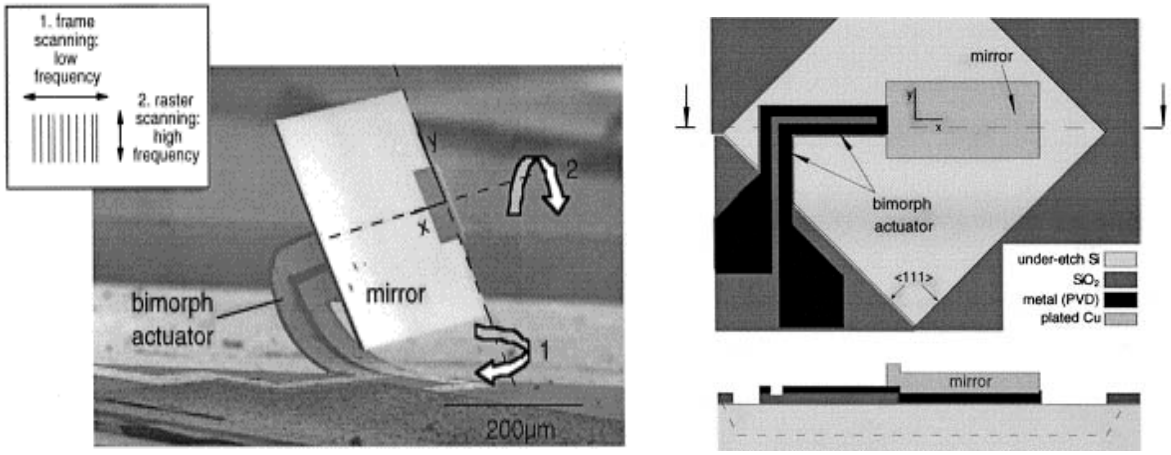

a) b)

Figure 1.6: a) SEM picture of the released bimorph actuator with mirror plate, there are two different motions indicated by 1 and 2 b) Two pictures, one in the upper refers to top view of bimorph actuator before releasing, and the lower one refers to the cross sectional view of the bimorph actuator.

There are two corresponding scanning directions, one is for raster scanning at 1345Hz showed as 1 in Figure 1.6a, the other is frame scanning at 10Hz showed as 2 in Figure 1.6b.

1.1.3 Telecommunication Applications

MEMS technology has served telecommunication industry since MEMS was launched into commercial market. High precision and compactness requirements make optical MEMS devices a fundamental part of telecommunication industry. Some examples of MEMS devices used in this field are presented hereafter.

1.1.3.1 Tunable Filters

For optical-networks and fiber-optic communication, tunable filters are indispensable tools. Briefly, tunable filters are used to pass desired wavelength while eliminating other wavelengths. Tunable MEMS devices propose high wavelength selectivity and

miniaturization for optical-networks and communication. Some examples of MEMS tunable filters for communication purposes are given in [20-22]. The illustration of a hybrid assembled Fabry-Perot filter with electrostatically actuated MEMS platform is given in Figure 1.7.

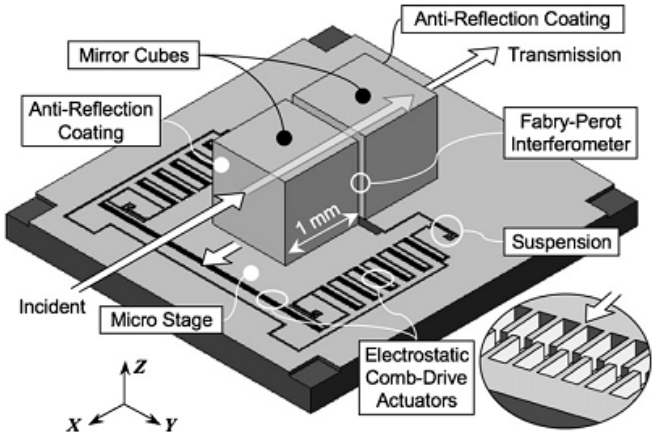

Figure 1.7: The illustration of hybrid assembled tunable filter on electrostatically actuated MEMS stage

As can be seen from Figure 1.7, the tunable filter consists a Fabry-Perot interferometer, comb drive actuator platform, proof mass carrying optical elements and mirror cubes.

1.1.3.2 VOA (Variable Optical Attenuator)

In fiber optic based communication, amplifiers are used to increase the signal level. The gain for different wavelengths shows a variety. Optical attenuators propose a solution to bring signals levels for each wavelength to a desired value. A good attenuator should have the characteristics of low loss, large dynamic range (ability to equalize the power levels for different channels). MEMS technology proposes low cost and compact devices

for optical attenuators. Electrothermal and electrostatic MEMS actuators were reported as VOA platform [23-24].

1.1.3.3 MEMS Optical Switches

To guide a bunch of information to a desired address, the path of the beam should be determined. In that purpose, optical switches can be considered crucial for telecommunication. MEMS based optical switches generally use mirrors to route the signal. Different actuation and configurations for optical switching are already in the literature [25-26].

1.2 Beam Steering with MLA Integrated MEMS Stages

Laser scanning is an integral part of modern imaging systems. Most of these systems utilize mirrors to steer the beam and thus require beam folding. For applications where size is a limiting factor techniques which could address these problems are therefore of great interest. Laser scanning based optical systems have been used in modern optical systems. Micro Lens Array (MLA) based scanning systems have been demonstrated by different research groups [27-28]. MLA based scanning systems can achieve a large amount of angular steering without necessity of large displacements [27]. These two facts taken together make it possible to create imaging systems with a small cross-sectional area. Laser scanning using MEMS can reduce the cost and complexity of the desired applications. For *In vivo* applications, miniaturization of the whole system is especially crucial. Beam steering with single microlenses using MEMS has been demonstrated in [28].The beam steering setup in this simple form , consisting only two MLAs , has a drawback in that only discrete diffraction angles can be addressed. But, importantly, it has been shown that by placing a movable Pre-Scan lens first in the optical train makes it possible to continuously address any point on the scanline [8]. The whole system proposes a miniaturized refractive

system consisting of 2 MLAs and 1 Pre-Scan Lens (PSL); all of which are desired to be vertically mounted on 2D MEMS stages for this project.

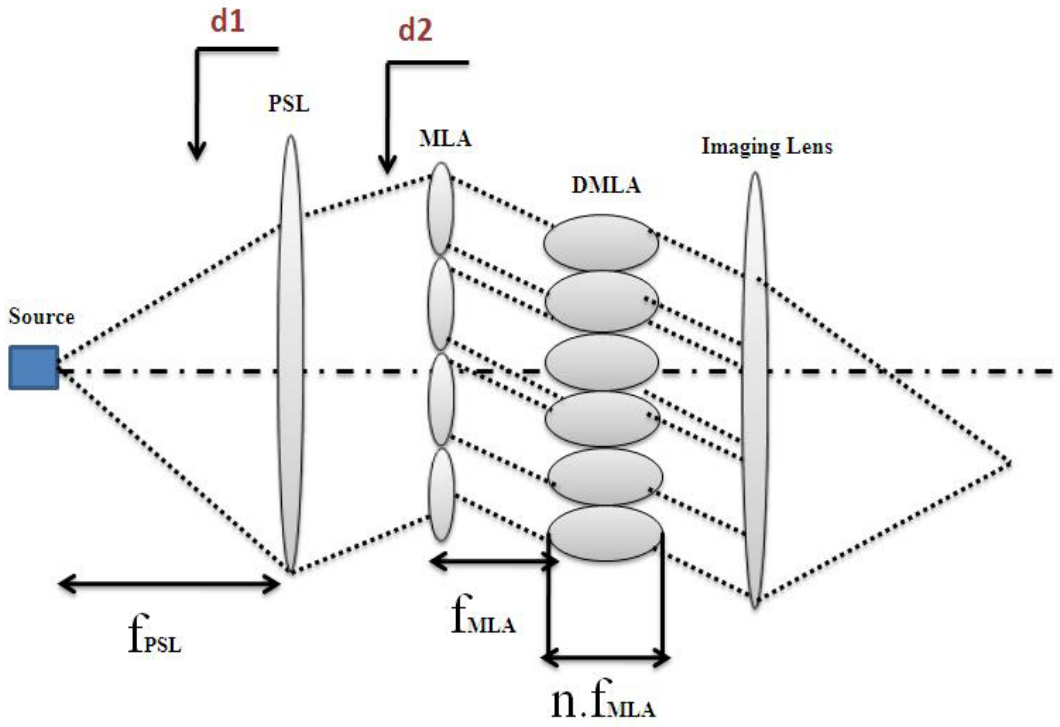

Figure 1.8: The depiction of optical configuration for MLA based beam steering

The Figure 1.8 depicts the whole optical system for continuous beam steering. While the first MLA is moving, second and third MLAs are combined and named as double MLA (DMLA). Two microlens arrays of DMLA must be separated with n.fMLA where n is the refractive index of the glass material. The discrete addressing problem is solved by using a movable PSL (Prescan Lens) in the system. Continuous beam steering with cascaded MLAs and theoretical background of the system is given in [27].

The angular beam steering stems from the relative lateral displacement of MLAs with respect to each other. The lateral displacement of the PSL is shown as d1 where lateral displacement of MLAs with respect to each other is given as d2 in Figure 1.8. The contributions of these lateral displacements to the angular steering can be written down as follows

$$\alpha = -r1/fPSL\,;\ \beta = r2/fMLA \tag{1.1}$$

$$\theta t = \alpha + \beta \tag{1.2}$$

Where *fPSL* and *fMLA* refer to focal lengths of the PSL and MLAs. The parameters of α and β are the beam scan angle constituted by displacements of PSL and MLA where θt refers to total scan angle.

1.3 Main Contributions of the Thesis

The main contributions of this thesis can be given as follows:

- *Design, development and characterization of a novel 2D MEMS actuator*: The actuator utilizes only one set of comb-finger for resonant actuation along out-of-plane axis and off-resonance actuation along in-plane axis. This is a novel MOEMS platform, on which MLAs were integrated hybrid for beam steering integration. Moreover, the actuation along both axes of the devices without MLA and MLA integrated devices are given. During design progress of the 2D actuators, different iterations were carried out to enhance the performance of the scanner. One of these is to eliminate bulk mass located in the outer frame of the actuator by defining circular hollows in the outer frame. Another enhancement is to design inner frame for hybrid assembly of the MLA with

taking mechanical performance specifications of the actuator. This project is funded by TUBITAK grant 106E068.

- *Design, development and characterization of a novel high frequency torsional scanner*: The actuator uses vertical resonant comb fingers for torsional actuation. Moreover, this new scanner utilizes different geometry with respect to similar examples in the literature. This new type of actuator are formed of multi frames to achieve low dynamic deformation and low air damping.

Chapter 2

2 MEMS Actuators

Actuators are the mechanical devices that utilize transfer of energy between different domains to make a translation or to control a system. MEMS actuators are forms of actuators in micro scale. In most cases, MEMS actuators transform one form of energy to a mechanical energy. In MEMS technology, there are vast amounts of different actuation mechanisms, including but not limited to, electrothermal, magnetic, electrostatic, piezoelectric and shape memory actuators.

This chapter mainly focuses on electrostatic actuation. The MEMS devices that are main interest of this thesis for this work rely on interdigitated comb finger actuation. In that manner, this chapter mainly describes on electro-mechanics of comb finger actuation for three different types of motion, which are in plane sliding motion, out-of-plane motion and torsional motion.

2.1 Electrostatic Actuation

Electrostatic actuation can be generated by utilizing coulombic forces between two oppositely charged. Electrostatic actuators have been used extensively in MEMS world, they are extensively chosen due to their low power consumption and also it is simple to fabricate two closely spaced gaps. There are different kinds of electrostatic actuation configurations including, but not limited to, comb drive [10, 15, 29], parallel plate [4, 30], scratch drive actuator[31].

For all cases, the electrostatic force generated by the actuators can be calculated from the stored energy (U_E). If the capacitance in charge for the system is *C*, and applied potential difference is *V*, then stored energy in the system is found to be

$$U_E = \frac{1}{2}CV^2 \tag{2.1}$$

Then the electrostatic force *F* is

$$F = -\nabla U_E \tag{2.2}$$

Assuming that *V* is fixed during actuation and the movement of the fingers is only in x direction, then the electrostatic force along x direction (F_x) is found to be

$$F_X = -\frac{\partial U_E}{\partial x} = -\frac{1}{2}V^2\frac{\partial C}{\partial x} \tag{2.3}$$

2.2 Interdigitated Comb Fingers

The electrostatic comb drive is one of the most popular and most widely actuators used in MEMS technology. These actuators are comprised of two different sets of comb fingers, which are stationary fingers and moving fingers. This type of actuation generates force by applying a potential difference between different sets of fingers. Rather than direct field as used for parallel plate actuation, comb finger mechanism utilizes fringing fields as the driving force for mechanical actuation. One of the key features of this actuation is to be able to increase number of comb fingers leading to decrease of voltage requirements for large displacements. Configurations of comb fingers for different types of translations are given in Figure 2.1.

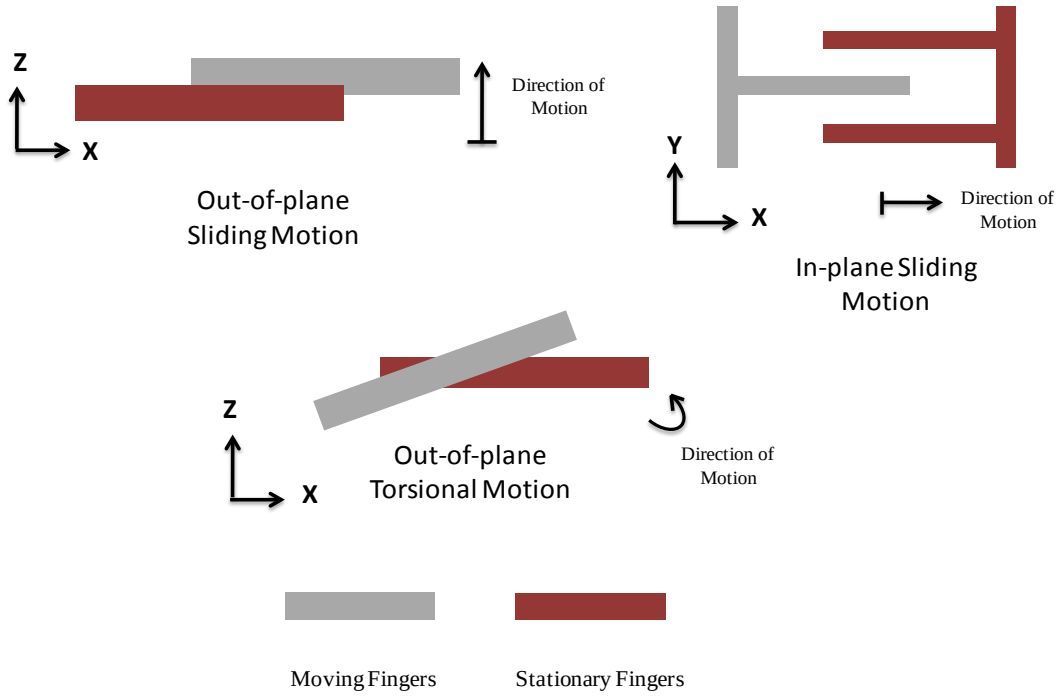

Figure 2.1: Translational configurations of comb fingers

2.2.1 In-Plane Translational Comb Actuators

In-plane translational comb actuators hold an important place for the applications demanding a linear and long range translation. The configuration for the in-plane translation utilizes two set of comb fingers where moving fingers are suspended to ensure a parallel motion to the fixed fingers. The gap between plates remains same during translation, which also proposes large translations. The schematic drawing of comb finger showing dimensional parameters are given in Figure 2.2.

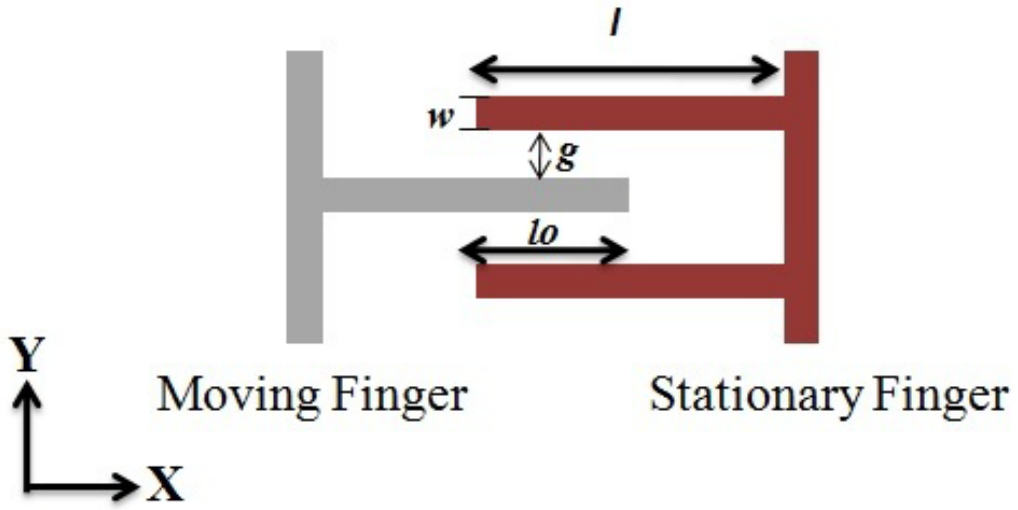

Figure 2.2: The illustration of comb finger and the parameters of the comb finger

As can be seen from Figure 2.2, the dimensions of *w*, *g*, *l*, *lo* refer to the width of comb finger, the gap between fingers, total length of the finger and lateral overlap of the comb fingers respectively.

In a given configuration, neglecting fringing fields, total capacitance of a comb finger set is given by:

$$Ctot = 2N\frac{\varepsilon(lo+x)t}{g} \tag{2.4}$$

$$F = \frac{1}{2}\frac{\partial Ctot}{\partial x}\,\mathrm{V}^2 \tag{2.5}$$

where N refers to number of total capacitances in the comb finger set and V refers the potential difference between the fingers. Capacitance change with respect to displacement for a typical comb finger in-plane translational actuator is obtained using ANSYS CMATRIX macro, see Figure 2.3a. Figure 2.3b shows how capacitance changes with displacement of the comb finger. Two different capacitive effects determine the shape of capacitance-displacement curve. When two fingers are almost fully engaged, the capacitance between tip of the moving finger and stationary frame becomes dominant. This effect can be seen at the left-hand side of the plot. After fingers start to get out of fully engagement, capacitance starts to decrease linearly. Non-linearity are seen only in a small portion of the curve, which indicates that fully engagement of the fingers occur in a short range of displacement. The linear portion of the curve also means that the capacitance change rate over displacement is constant and independent of displacement.

The actuation force is constant with the displacement but it is still non-linear with applied voltage. The force can be linearized with utilizing differential drive scheme in the case of configuration in which mechanical stages are actuated by two sets of comb fingers that are applying forces in opposite directions. The voltage configuration for this case is as follows

$$V_1 = V_{DC} - V_{AC} \sin wt \tag{2.6}$$

$$V_2 = V_{DC} + V_{AC} \sin wt \tag{2.7}$$

Then the resultant force becomes

$$F = F_1 - F_2 = 4N \frac{\varepsilon t}{g} V_{DC} V_{AC} \sin wt \tag{2.6}$$

If V_{DC} is kept constant, resultant force is linearly dependent on time varying voltage difference.

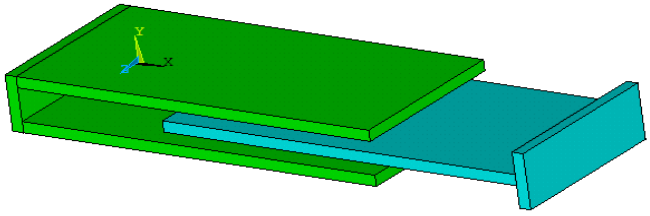

a)

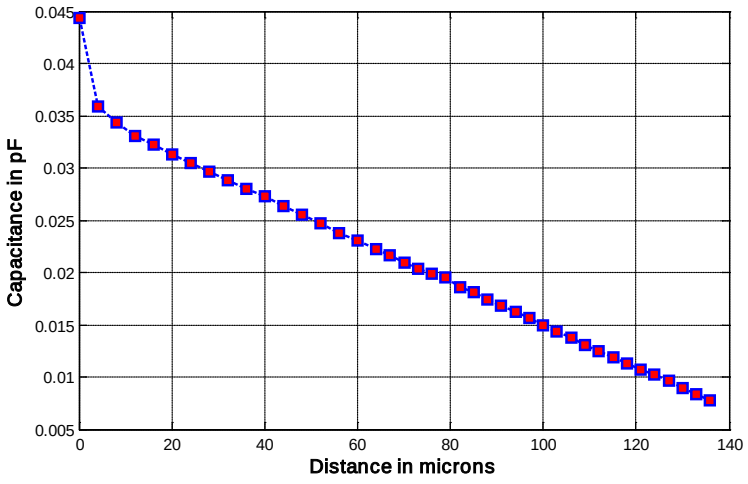

b)

Figure 2.3: a) FEM model used to extract capacitance versus displacement characteristics b) ANSYS simulated capacitance versus displacement characteristics of a in-plane translational comb finger. The parameters used for simulation : w = 5μm, g =5μm, l=160μm , lo=95μm

This linear characteristics of in-plane translational comb actuators are crucial and good for applications like tunable optical detectors [32], tunable cavities [33] and optical switches [34].

2.2.2 Out-of-Plane Translational and Torsional Comb Actuators

Comb actuation promises out-of-plane actuation and torsional actuation without any need of non-uniformity in the structure geometry. Depending on structural configuration, comb actuators can produce out-of-plane or torsional translation in the corresponding resonance frequency. This type of configurations has been used particularly for torsional micromirror devices [11, 35-36] . The 2D scanner and torsional scanner that are described in this thesis utilize comb actuators for out-of-plane and torsional translation respectively.

Capacitance change with respect to displacement for a typical comb finger in-plane translational actuator is obtained again using ANSYS CMATRIX macro, see Figure 2.3a. Figure 2.3b shows how capacitance changes with displacement of the comb finger. The capacitances curve for out-of-plane and torsional actuators are similar, and therefore, they are treated together. As can be seen from Figure 2.4b, the capacitance has its peak value at its rest position; rest position refers to the case where the fingers are totally engaged. After the rest position, capacitance starts to decrease in a faster manner. This decrease of the capacitance starts to slow down after the fingers are totally disengaged. Both torsional and out-of-plane translational modes have displacement dependent electrostatic force (torque) and their governing second order equations are non-linear [37].

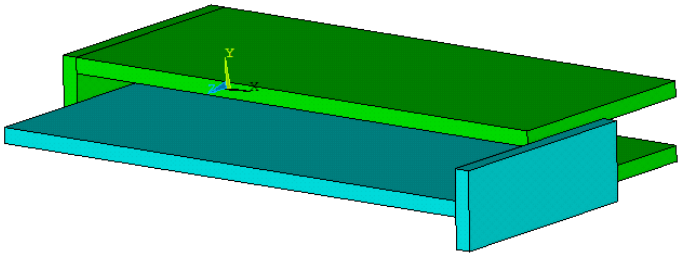

a)

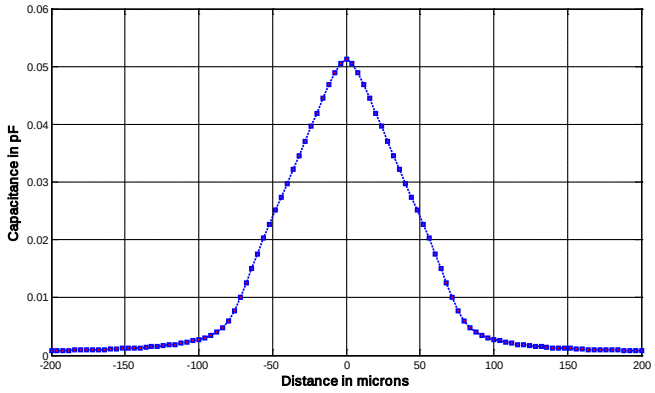

b)

Figure 2.4: a) FEM model used to extract capacitance versus displacement characteristics b)ANSYS simulated capacitance versus displacement characteristics of a out-of-plane translational comb finger. The parameters used for simulation: w = 5μm, g =5μm, l=170μm, lo=160μm, and device thickness=75 μm

Due to the symmetry of comb fingers, DC actuation is not possible. In other words, symmetry in the comb finger geometry allows vertical translation in resonance only. To be able to make translation in DC, different offset geometries have been used in comb finger designs. Piyawattanametha et al. developed angular vertical comb actuators to actuate the

scanner in two different dimensions by applying voltage in DC [38]. Two examples of out-of-plane comb actuators are given in Figure 2.5.

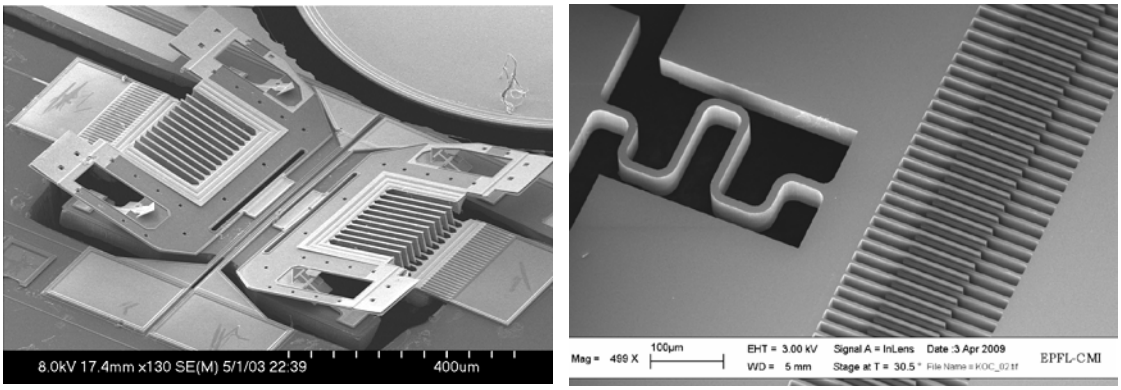

a) b)

Figure 2.5: a) Angular vertical comb finger actuator for 2D torsional actuator [38]
b) Uniaxial comb-finger actuator for out-of-plane actuator

Figure 2.5a shows an example of using offset geometry to actuate torsional mode in DC, with this configuration The maximum mechanical scanning ranges are (at 55 DC Voltage) and (at 50 DC Voltage) for the inner and the outer gimbals, respectively. Figure 2.5b is the SEM picture of 2D scanners described in this thesis. There is no unsymmetrical between the fingers and the out-of-plane actuation was achieved in resonance.

Chapter 3

3 2D MEMS Stages

Electromechanics and electrostatic characteristics of different electrostatic actuators are investigated in previous chapter with an emphasis on comb finger actuators. A novel 2D electrostatic MEMS actuator that utilizes uniaxial comb finger geometry is presented in this chapter. Firstly, device geometry overview is described in detail, after that Finite Element Model (FEM) results of the stage without MLA and stage integrated with MLA are presented in this chapter. After these, microfabrication steps and results are described. Later, the experimental results of 2D stage without MLA and MLA integrated 2D MEMS stage are given. Lastly, the beam steering demonstration is presented in this chapter.

3.1 Device Geometry Overview

The device consists of two cascaded frames, each suspended by four flexures. The simplified drawing of the whole device is given Figure 3.1.The dimensions of the outer frame are 4.2 mm × 2.0 mm and its four flexures are all parallel to the longer side, each 80 μm long and 10μm wide. The inner frame has dimensions of 1.15 mm × 0.3 mm. The inner frame is 300μm × 1150μm and is suspended by two straight and two folded flexures. The straight flexures are each 850μm and are parallel to the outer flexures, while the folded flexures are 800 μm. The four inner flexures are 12μm wide. The outer frame is perforated with holes to decrease the weight and the air pressure (and thus increase the effective quality factor). The movable fingers in the electrostatic comb-drive are 5μm × 160μm and placed on each side of the device. And the initial overlap of the fingers is 95μm. The spacing between combs is 5 μm. The vibration modes of interest are in-plane sliding mode and out-of-plane bending mode. The low-frequency in-plane motions of the

combs move the MLA stage by the same amount. For out-of-plane actuation, the amounts of deflections on the MEMS stage are not distributed equally. More clearly, the desired mode is out-of-plane bending mode and the peak deflections occur around in the middle of the frame, where MLA is also placed.

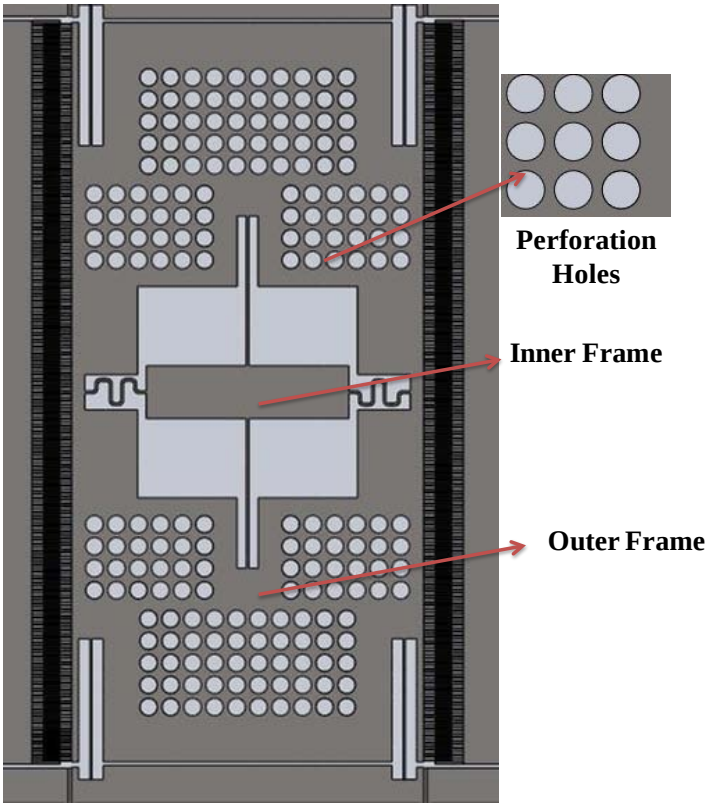

Figure 3.1: The schematic drawing of front side of 2D MEMS Stages

As can be seen from Figure 3.1 , the inner frame is placed in the middle of the scanner and there are 196 perforation holes placed in the outer frame. Comb fingers are placed at the two sides of the scanner.

3.2 Mechanical Design

There are two main constraints while designing the stages. Firstly, the device should be capable of deflecting along each axis, in-plane and out-of-plane motion, with an amount of 50µm without exceeding stress limit of 1.5GPa.

Secondly, the vibration modes should be arranged in the manner that the in-plane sliding mode should be placed as the first mode to enable DC actuation and the resonant-actuated out-of-plane mode should be well-separated from the other vibration modes.

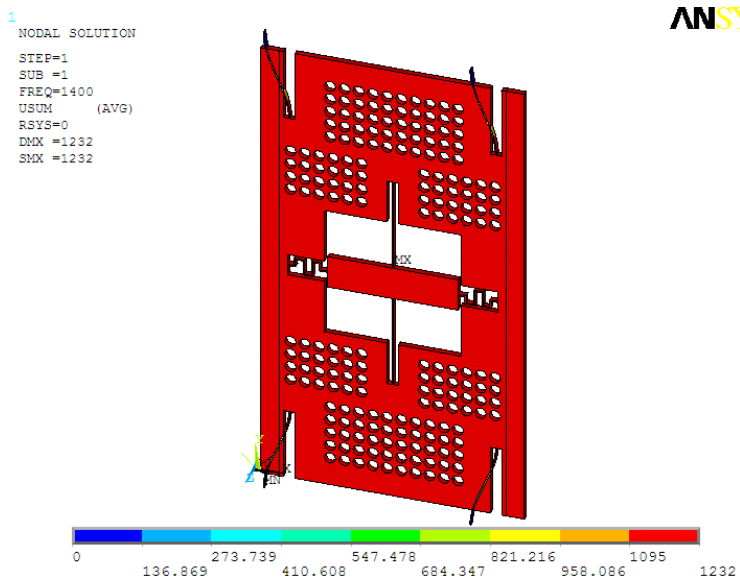	**1st Mode** **In plane sliding motion along x-axis (1400Hz)**

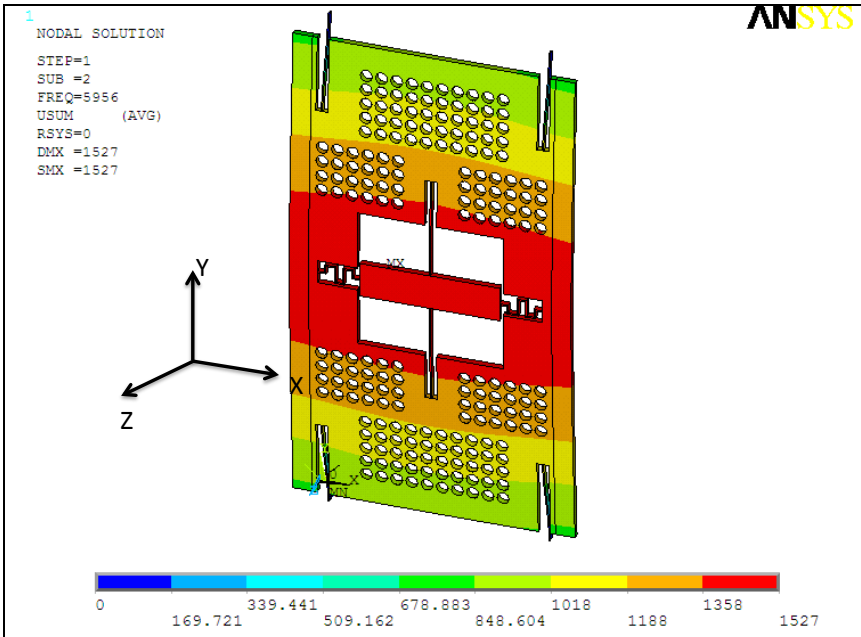	**2nd Mode** **Out of plane bending motion along z-axis (5956Hz)**
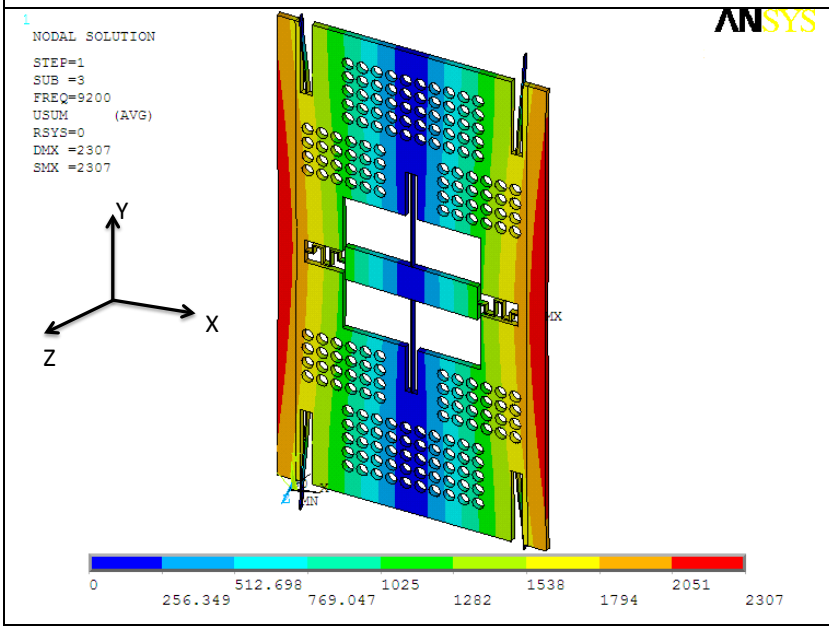	**3rd Mode** **In phase torsion mode around y-axis (9200Hz)**

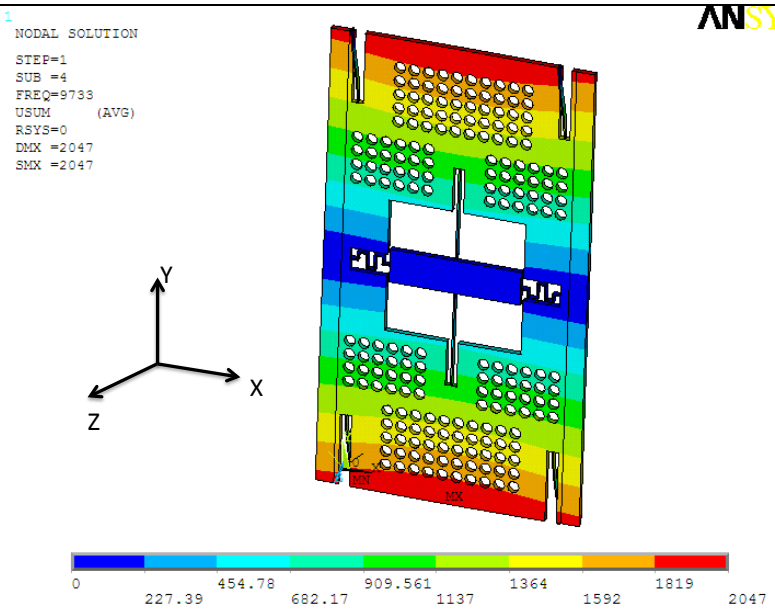	**4th Mode** **In phase torsion mode around x-axis (9733Hz)**
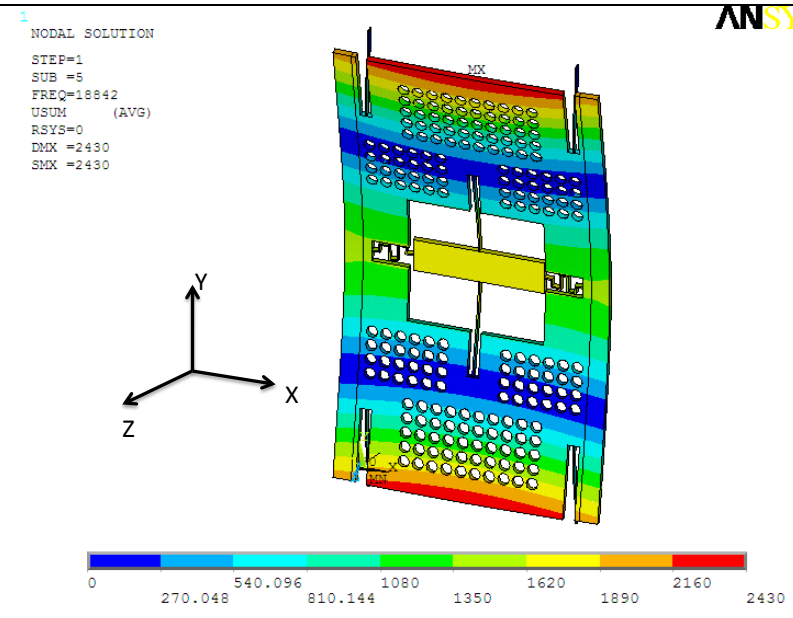	**5th Mode** **Out-of-phase bending mode (18842 Hz)**

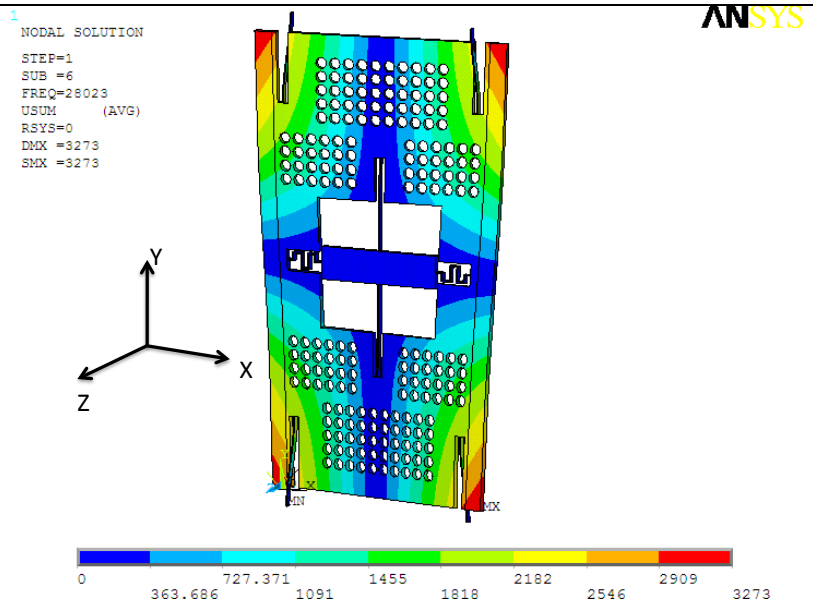	**6th Mode** **Outer frame rocking mode** **(28023 Hz)**

Table 3.1: The first six resonant modes of 2D MEMS stage without MLA

As can be seen from Table 3.1, the first mode is in-plane sliding motion in which inner frame and outer frame are making the same amount of translation along x-axis in phase. The same amount of deflection stems from the fact that folded flexure limits inner frame's in-plane translation freely; these folded flexures are designed to provide a safe MLA mounting. The second desired motion is out-of-plane movement which is also placed as the second resonant mode. In this mode, the device is showing a bending motion along z-axis. The resonance frequency corresponding to out-of-plane bending motion is approximately 5960Hz. When looking the modal results of out-of-plane motion**,** the device make different amount of displacements on different areas of the device. The stage makes its peak deflections around inner frame.

Third mode and fourth modes are torsion modes of the stage. In the third mode, the stage is deflecting around x-axis while it is deflecting around y-axis in the fourth mode.

These two torsion modes show in-phase characteristics, in which the inner and outer frame is making the translations with no mechanical phase difference. Fifth mode is another bending mode similar to the second mode, but the difference between two modes in terms of motion characteristics is that the maximum deflection points are different. In the fifth mode, the peak deflections are clustered around upper and lower edges of the device while in the second mode the peaks are seen around inner frame. The sixth mode is outer frame rocking mode which has a resonance frequency approximately 28023Hz.

Similar analyses are pursued for also the model for showing MLA integrated MEMS stages. The first six modal analysis results corresponding to 2D MEMS stage integrated with MLA is given in Table 3.2

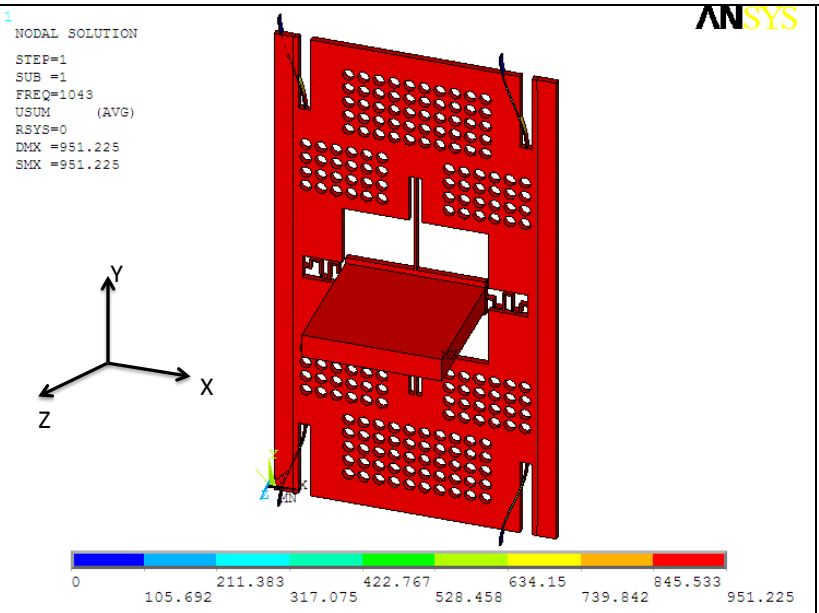	**1st Mode** **In plane sliding motion along x-axis** **(1043Hz)**

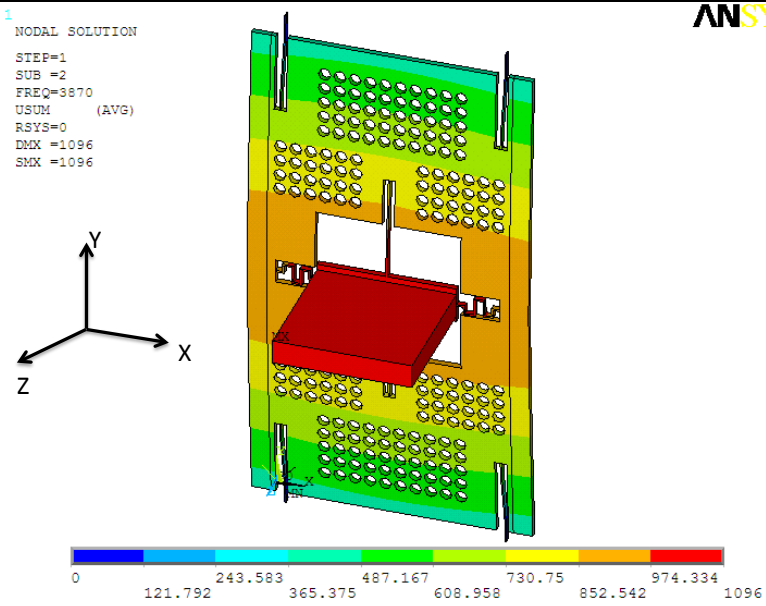	**2nd Mode** **Out of plane bending motion along z-axis** **(3870Hz)**
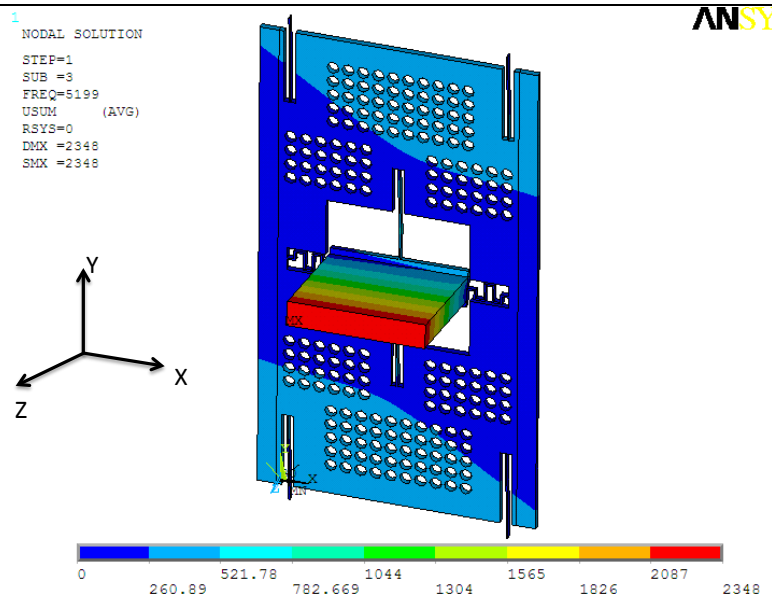	**3rd Mode** **Only inner frame rotating around x-axis** **(5199Hz)**

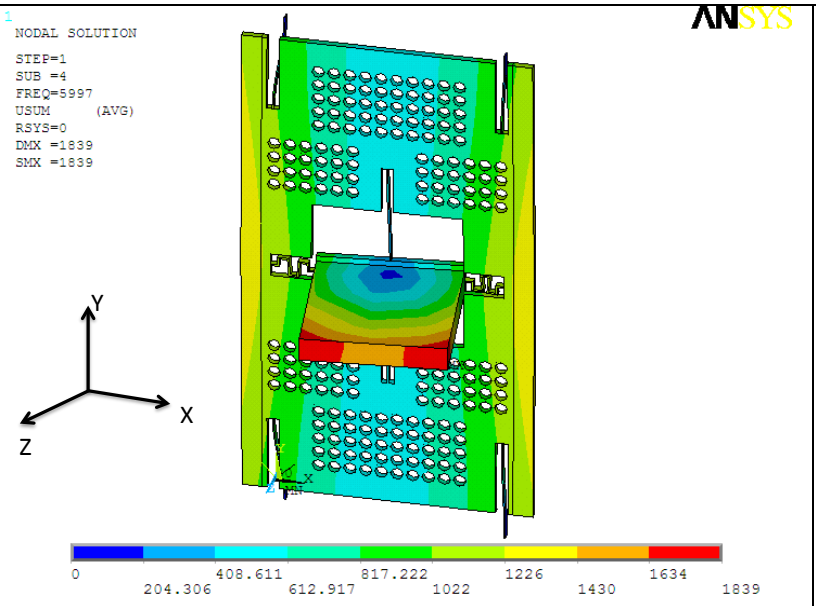	**4th Mode** **In plane rocking mode (5997Hz)**
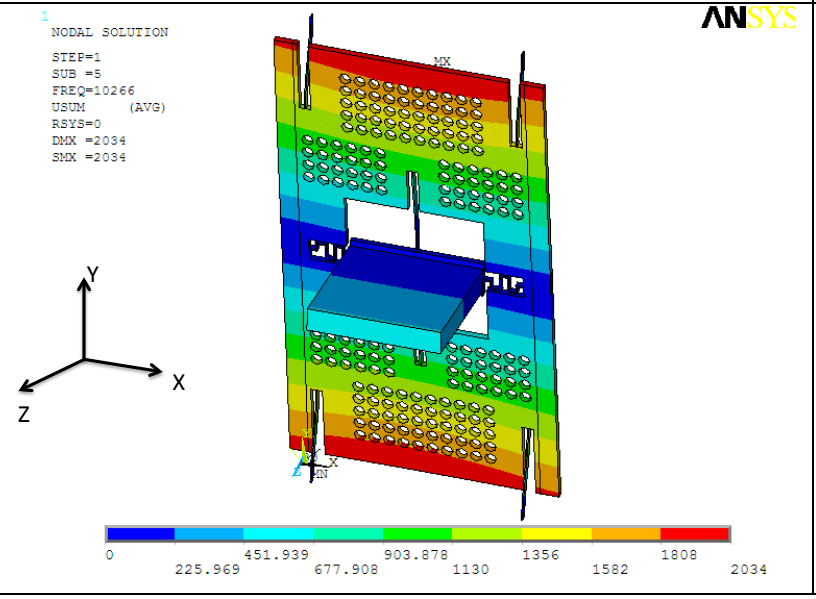	**5th Mode** **In phase torsion mode around x-axis** **(10266 Hz)**

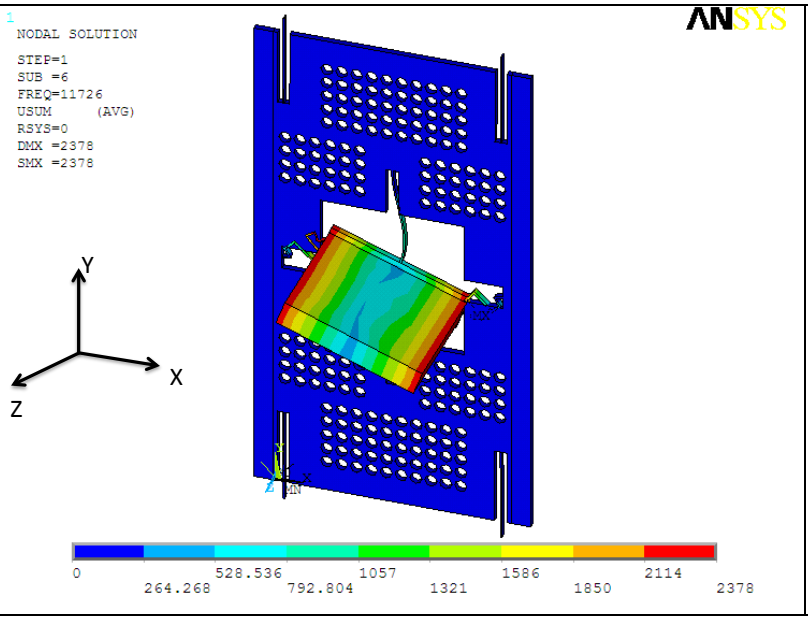	**6th** **Only inner frame rocking mode** **(11726 Hz)**

Table 3.2: The first six resonant modes of 2D stages integrated with MLA

As can be seen from Table 3.2, similar to the results presented for the device without MLA, again the first two modes belong to in-plane sliding motion and out-of-plane bending motion respectively. When the results shown in two tables are compared, there are some prominent differences. More clearly, the modes except first two modes show a significant difference in the case of MLA integration with respect to the case of only 2D MEMS stage. These differences stem from large mass addition, which leads torsion and rocking modes to get closer to the desired two modes.

3.3 Stress Load

The electrostatic MEMS stage should satisfy maximum stress limit, 1.5 GPa, at desired amount of deflections. While engineering mechanical design of the scanner to satisfy stress limits, frequency separation and working frequency specifications are also taken into

account. As described in the previous parts of this chapter, out-of-plane motion is desired to be actuated in resonance while in-plane motion is desired to be actuated off-resonance. One of the goals is to actuate in both directions simultaneously. In that sense, two different stress load analysis were pursued for translations along different axes.

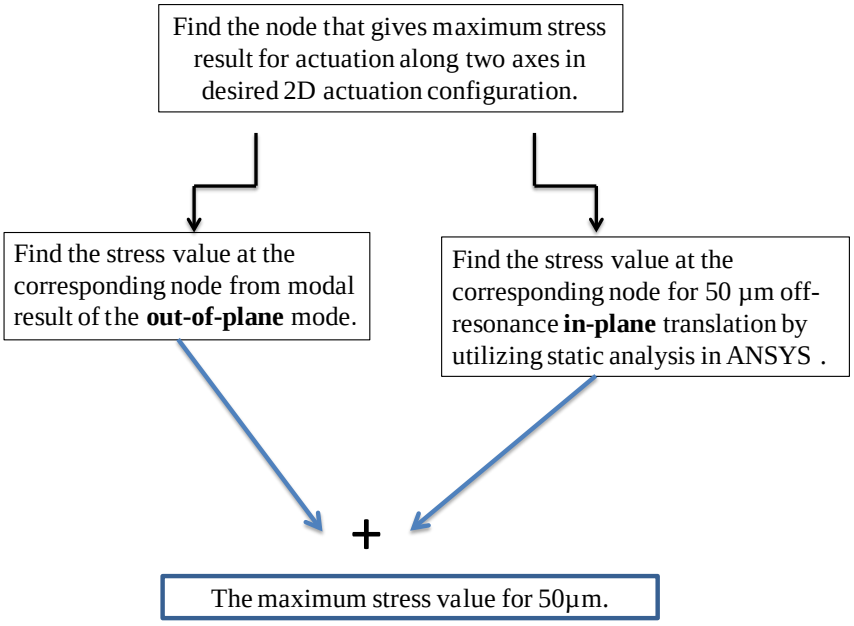

Figure 3.2: The progress for finding maximum stress value for 2D actuation

To be able to find maximum stress values at desired deflections for two axes, stress values for two different translations at the node that gives total maximum stress value are added. For the sake of easy comprehension, the procedure for finding maximum stress value for 2D actuation, progress is schematically illustrated in Figure 3.2. To be able to find stress distribution for off-resonance in-plane translation, static analysis is pursued, see Figure 3.3. For finding out-of-plane mode stress distribution corresponding to 50µm deflection is found by utilizing modal analysis and elemental results of the mode, Figure

3.4. The first step is to find the locations that have high stress distribution. High stress values are generally located the connection points between outer springs and outer frame, these points refer to where maximum elongation takes place. It should be noted that maximum values that got from analysis (which are seen as red on the bars at the below of stress distribution figures) occur at areas where constitute infinite stiffness. This unrealistic infinite stiffness phenomenon stems from Degree of Freedom (DOF) modeling of the parts of the scanner that connects the stage to the bulk area; the constraints on the displacement of the areas connecting to the bulk are given as zero. With taking this issue into account, the stress values corresponding to these points are not taken into account for stress calculation. Infinite stiff locations and stress distributions of these points are shown in Figure 3.5.

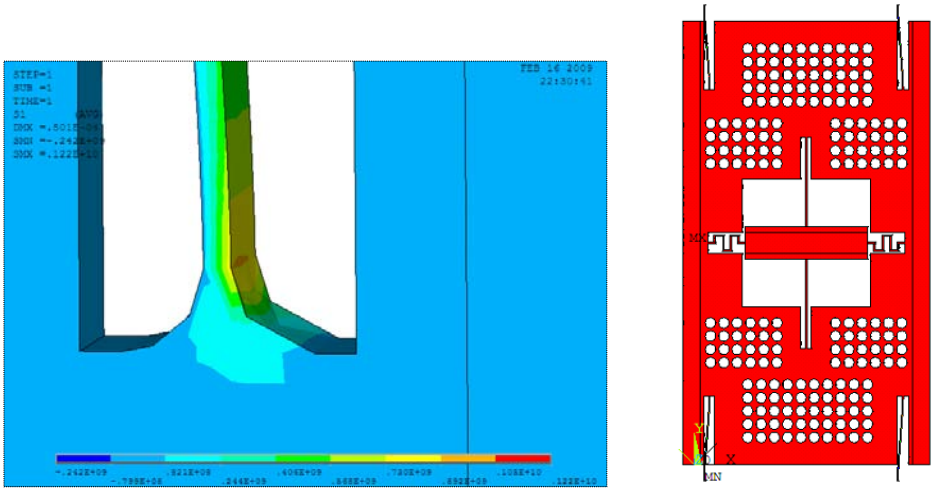

Figure 3.3: 50µm in-plane translation static analysis results

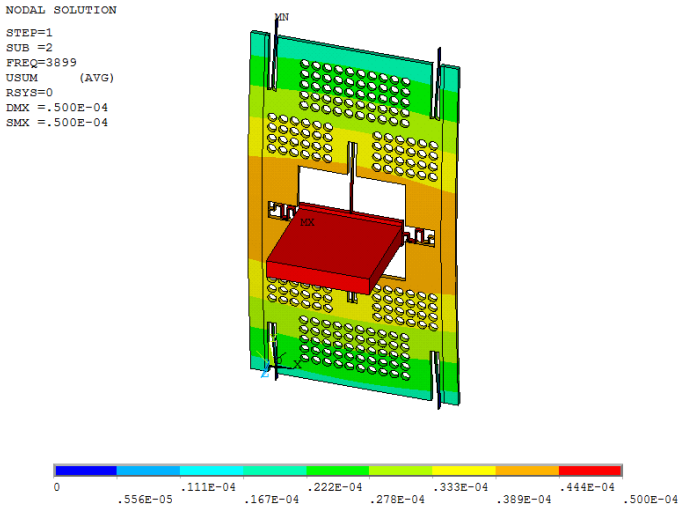

a)

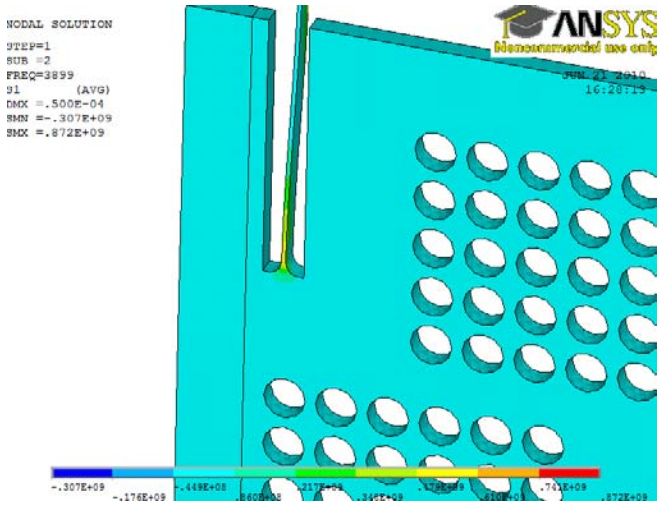

b)

Figure 3.4: a) The scaled nodal displacement distribution for out-of-plane mode, at where maximum deflection is scaled to 50μm b) The stress distribution for corresponding mode and 50μm maximum deflection along out-of-plane axis.

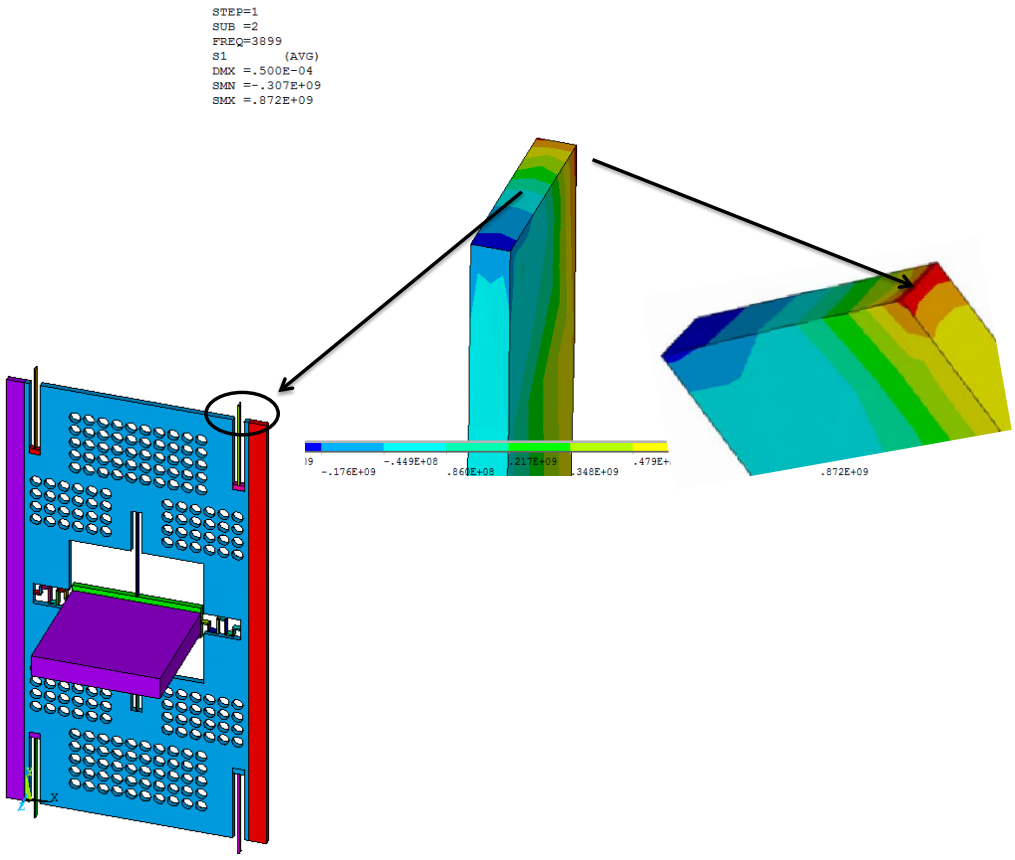

Figure 3.5: Infinite stress locations and corresponding stress distributions

Pursuing the progress as illustrated in Figure 3.2, the resultant stress values is found to be around 1.38 GPa.

3.4 Microfabrication

Devices were fabricated on Silicon-On-Isolator (SOI) wafers with a 380 µm thick handle layer, a 2 µm thick buried oxide (BOX) and a 50 µm device layer, the latter determining the thickness of the entire mechanical structure. In Figure 3.6 the process flow of the three mask fabrication is given. Resist is used as etch mask in all cases and contact

alignment is used for all photolithographic pattern transfers. Mask 1 is used for patterning of metal, which is needed for wire bonding and electrical connections, Mask 2 is used for front side device definition and Mask 3 is for etching handle layer. Au/Cr (130/15 nm) is blanket deposited onto the device side of the wafer by sputtering (Figure 3.6b). Following photolithography using Mask 1, the metal is patterned by wet etching (Figure 3.6c). Next step is to transfer the front side device definition from Mask 2. 5 µm thinned AZ9260 positive resist is used as an etch mask during the front side DRIE (Deep Reactive Ion Etching) process, which defines the entirety of the mechanical structure in the device layer (Figure 3.6d). The etching is stopped at the BOX (Buried Oxide) layer. The last lithography step is performed after first DRIE step, using 10 µm AZ9260 resist and double sided alignment to transfer the backside windowing pattern (Mask 3). The backside windows and dice-trenches are formed by a second DRIE, which also is stopped at the BOX layer (Figure 3.6e). The final device release is achieved through oxide etch in HF vapor (Figure 3.6f). Hybrid integration of MLA on the MEMS stage is done after the dicing. The mounting was performed manually using microstages, the lens being fixed with UV-curable epoxy (Figure 3.6g).

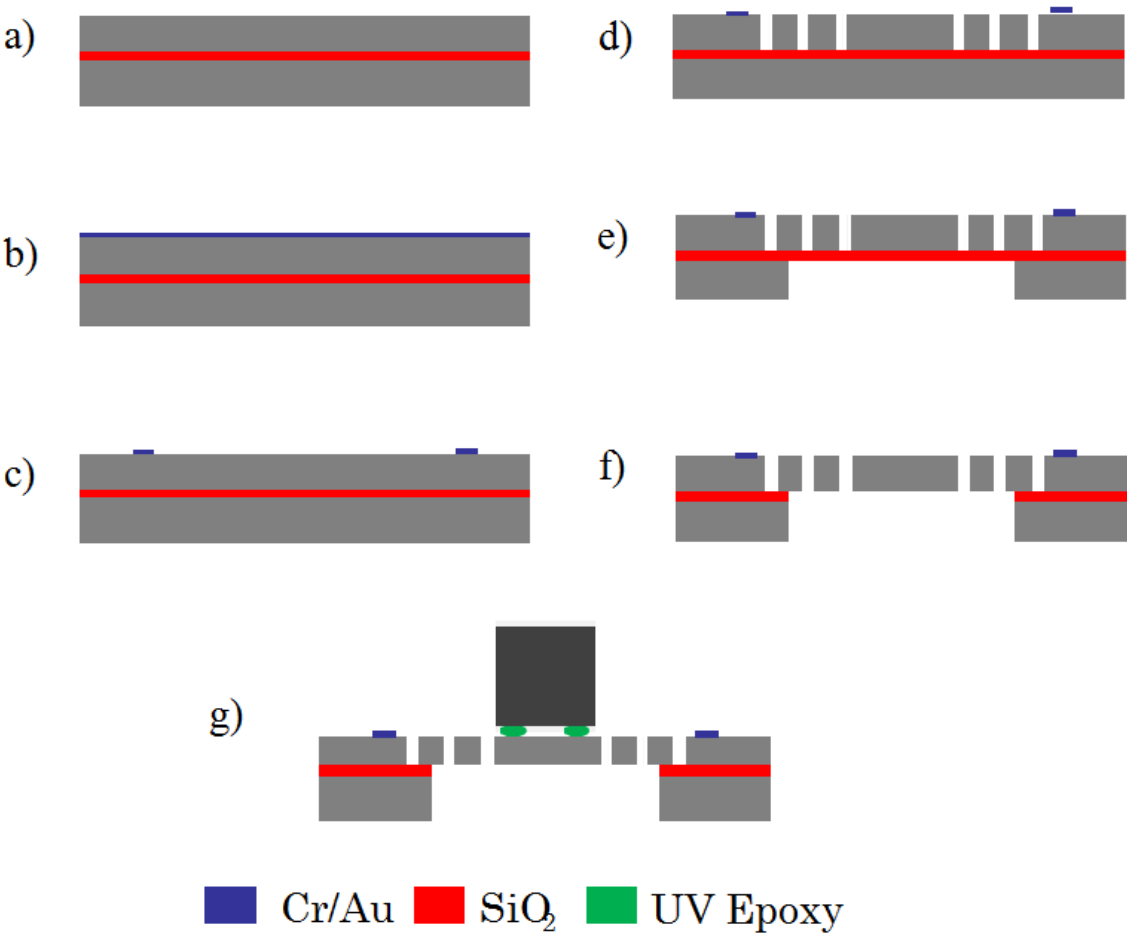

Figure 3.6: Process flow

The mechanical performance of the scanner is strongly dependent on the front side etching. During this step, the hinges and springs are defined, which constitute the main parameters affecting mechanical performance of the actuator. In that manner, the etch rate

for the first DRIE step should be homogenous on different portions of the wafer not to lead overetch or underetch on the wafer. To achieve a homogenous etch rate on the wafer, some extra volumes were defined during front side etching. These volumes, see Figure 3.7, were eliminated during the last etching step.

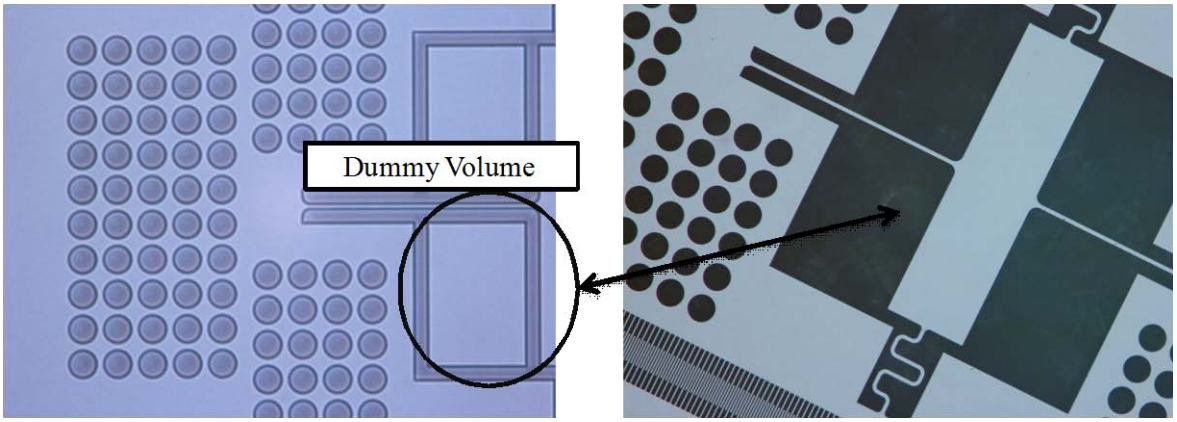

Figure 3.7: The microscopic snapshots showing inner frame after first DRIE step (left hand side) and after release (right hand side)

The differences of front side view after first DRIE step and after release are shown in Figure 3.7. As can be seen from the left hand side of the figure, there are rectangular volumes that surrounding inner frame after first DRIE step. These volumes are defined during first DRIE step; they hang on only BOX layer. During the etching of the BOX layer underneath these volumes, they are released.

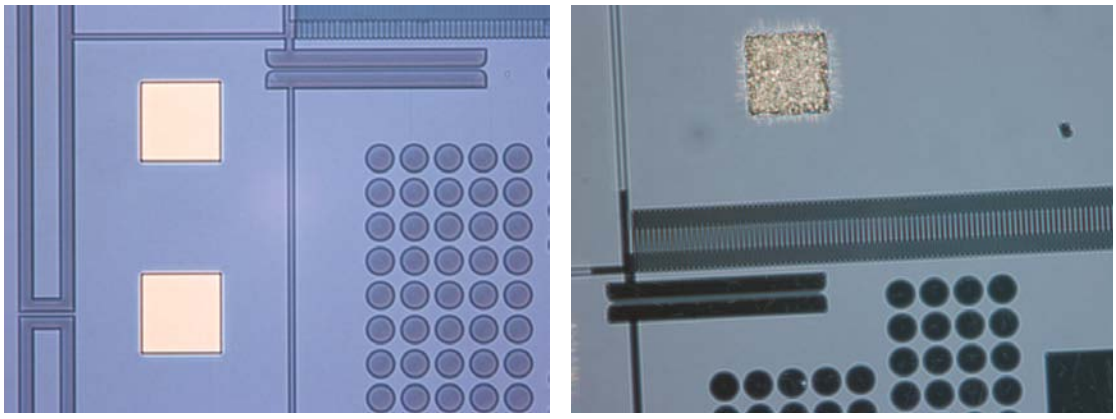

a) b)

Figure 3.8: a) Metal pads before last lithography step b) Metal pads after releasing

During the first run of the fabrication, there were some problems encountered. One of these problems is the metal pad's quality, there is a significant difference on the metal pad's quality before front side etching and after releasing, see Figure 3.8. This problem occurs during stripping AZ9260 10 µm resist that is used for last lithography step. We used wet removers to strip resist in first two lithography steps, in which thinner resists are used. For stripping AZ9260 10 µm resist, Tepla 300^{TM} Oxygen Plasma Stripper is used. During this stripping step, blanket deposited chromium lying underneath gold got into reaction with oxygen plasma. In later runs, the problem was overcome by arranging the power level and process time in oxygen plasma stripper. SEM pictures of the released 2D MEMS actuators are given in Figure 3.9. The problem related to the metal pads can be seen also in Figure 3.9b.

As described earlier, MLA mounting onto MEMS scanners was achieved using UV curable epoxy. The pictures of MLA integrated MEMS scanners were given in Figure 3.10.

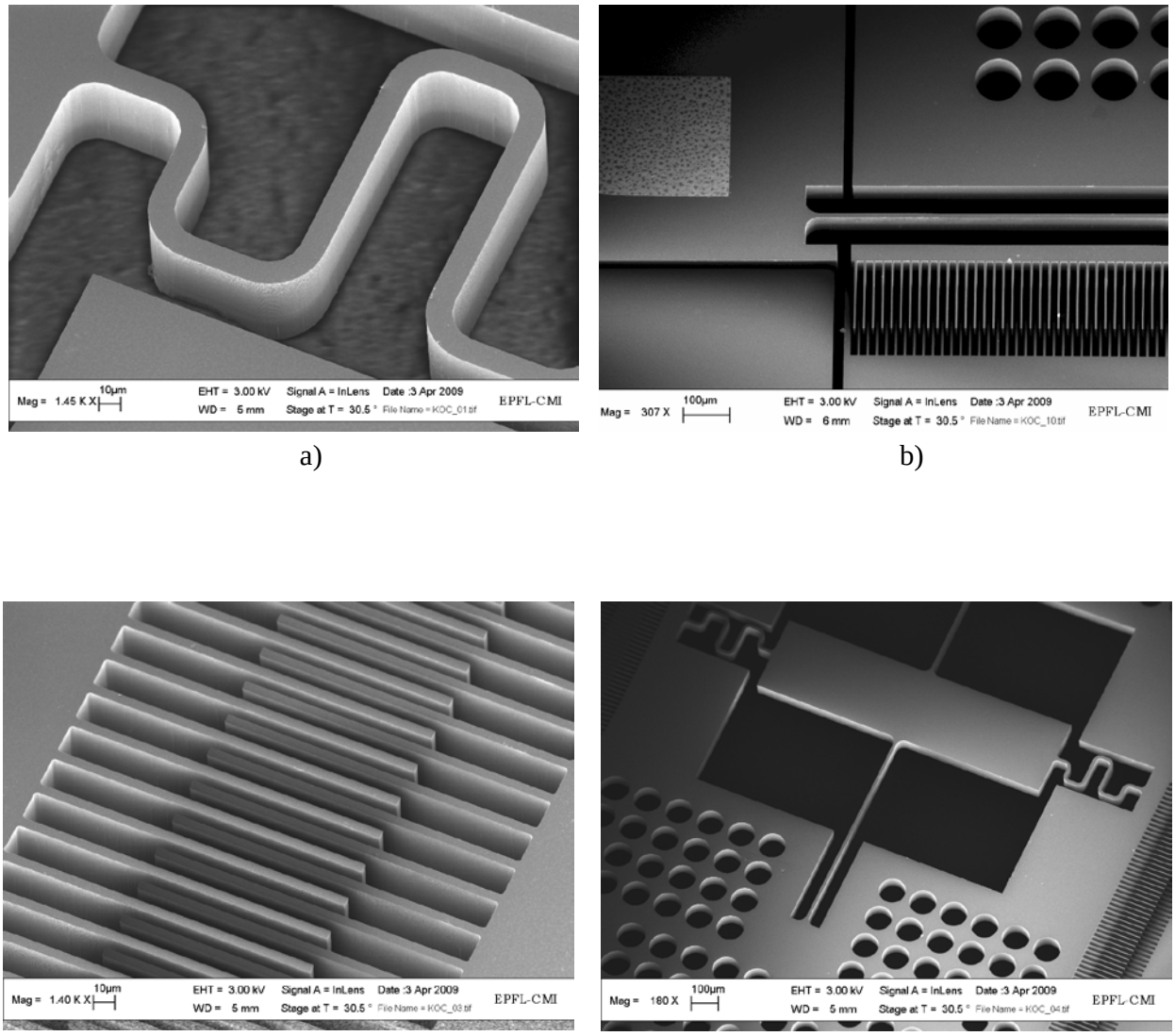

Figure 3.9: SEM pictures of 2D scanners a) Inner frame's folded flexures b) Metal pads and outer flexure c) Comb fingers d) A general top view showing front side of the scanner

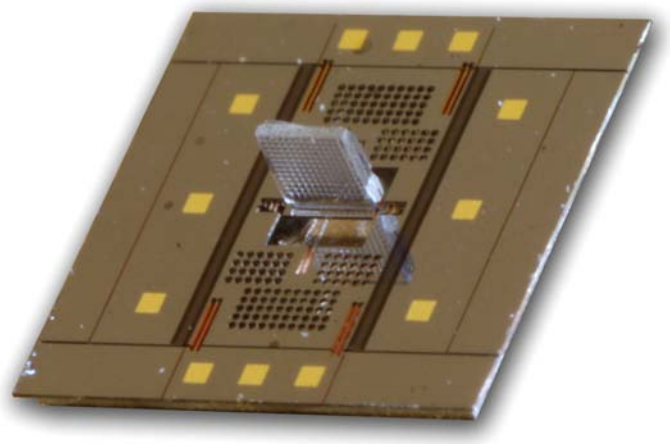

a)

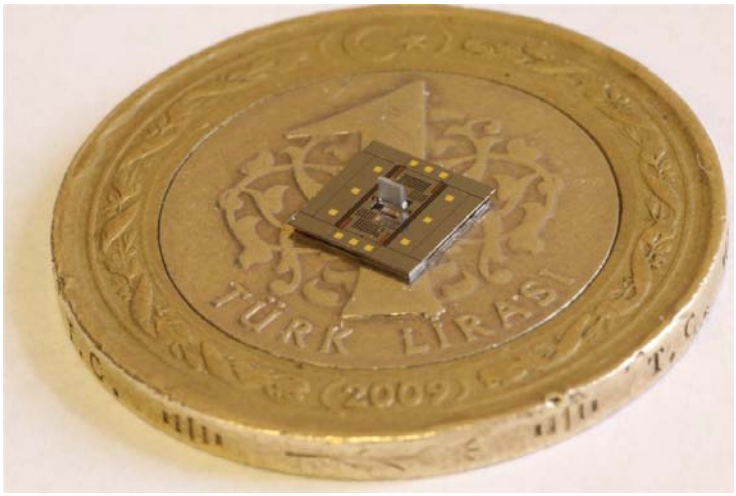

b)

Figure 3.10: a) A close-up picture of MLA integrated MEMS stage b) MLA integrated MEMS stage on 1 Turkish Lira

3.5 Experimental Results

The resonance modes of the devices are located with laser doppler vibrometer (LDV, Polytec, OFV-2500 and OFC-534). While this technique only measures movements parallel to the beam of the device, pure in-plane movements can also be detected by tilting the instrument relative to the silicon surface. The LDV is also used to quantify the out-of-plane movements of the device. For quantification of in-plane motion camera output has been utilized. Hereafter, experimental results will be presented in two main parts, which are out-of-plane characterization and in-plane characterization. In Figure 3.11, a close-up picture of electrically probed device is given and voltage configuration is illustrated in the picture as well. Characterization of all of the 2D stages is executed in ambient air.

3.5.1 Out-of-Plane Actuation

The dynamic behavior of the out-of-plane actuators varies with the excitation signal and can be modeled with the second-order differential equation. For the stage without the mounted MLA, it has a very good fit with the resonance modes observed with LDV-measurements done in this way. The manual mounting of the MLA, however, brings an uncertainty to the weight distribution of the finalized device. Because of this, certain modes for the mounted cannot be predicted with the same precision. In future work, the alignment of the MLA could be improved by etching a carefully sized groove into which the vertically mounted MLA could be placed.

Because of the geometry of the out-of-plane bending mode of the stage, the change rate of capacitances will vary with time amount of disengagement, in turn making the force dependent on the momentary disengagement. The system therefore constitutes a nonlinear parametric oscillator. Certain behaviors are expected from such a system. Firstly parametric oscillators display subharmonic oscillations located at $2f_r/n$ where where f_r is

the mechanical resonance frequency of the system, and n is a positive integer [39-40]. The amplitude decreases with increasing n, because of this n=1and n=2 tend to be the only ones found in ambient atmosphere. Note that the formula gives the usable actuation frequencies, the mechanical action of the oscillator will in all cases be close to f_r. Fitting with this model the out-of-plane mode exhibit maximum displacement when actuated at double the natural frequency. In that sense, the electrical actuation frequency applied for out-of-plane motion is $2f_r$. Secondly a characteristic hysterical frequency response is expected for these systems. Two different jump frequencies $f_1$and f_2 are encompassing an unstable region and found for back-sweep and forward-sweep of the frequency, respectively ($f_2 > f_1$). The placement of the two jump frequencies are dependent of the actuation voltage, which obviously means that that drive frequency has to be chosen according to the voltage used. The voltage configuration for out-of-plane actuation is given as:

$$V_1 = V_{DC} + V_{AC}\sin(wt) \quad (3.1)$$

$$V_2 = V_{DC} + V_{AC}\sin(wt) \quad (3.2)$$

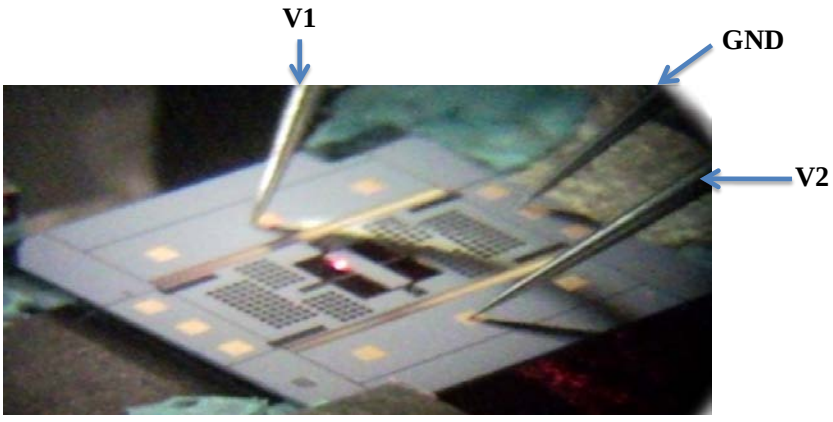

Figure 3.11: The electrically probed 2D MEMS stage and corresponding voltage configurations

For the 2D MEMS stage without MLA, 51,6 µm peak-to-peak deflection is obtained at around 6615 Hz with an applied voltage of 158 Volt peak-to-peak during forward sweep, see Figure 3.12, the same amount of deflection (51,6 µm peak-to-peak) is obtained at around 6595 Hz with an applied voltage of 172 Volt peak-to-peak , see Figure 3.13. It should be noted the amount deflections declared in the figures of this chapter are all peak-to-peak values.

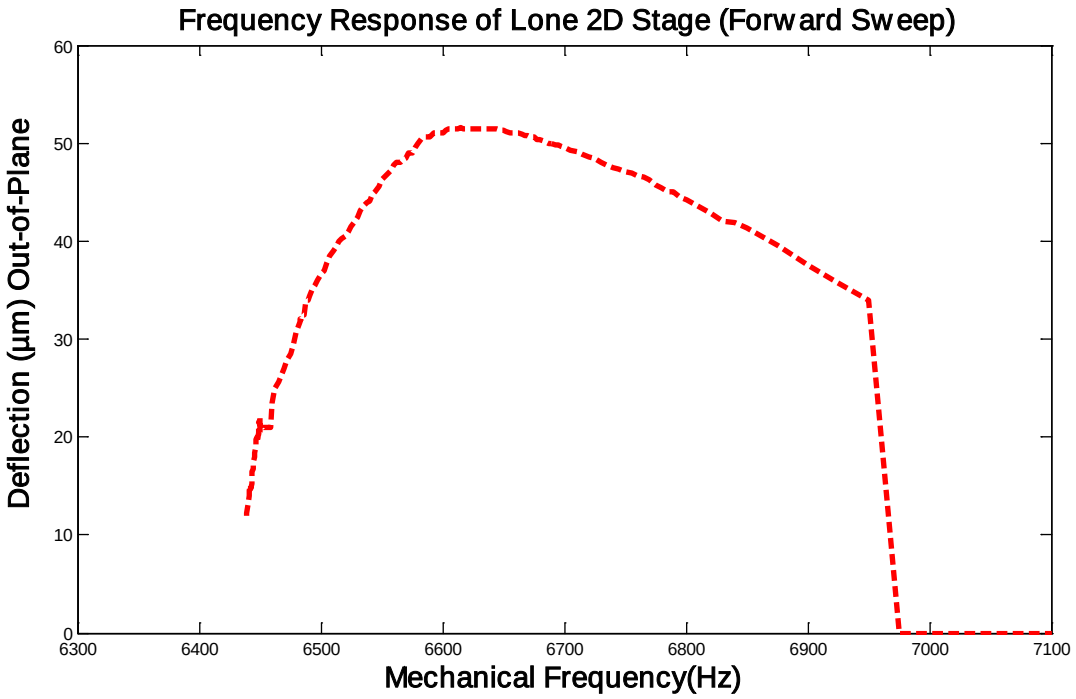

Figure 3.12: Frequency response of 2D MEMS stage without MLA (forward sweep) with applied voltage of 158 Volt peak-to-peak

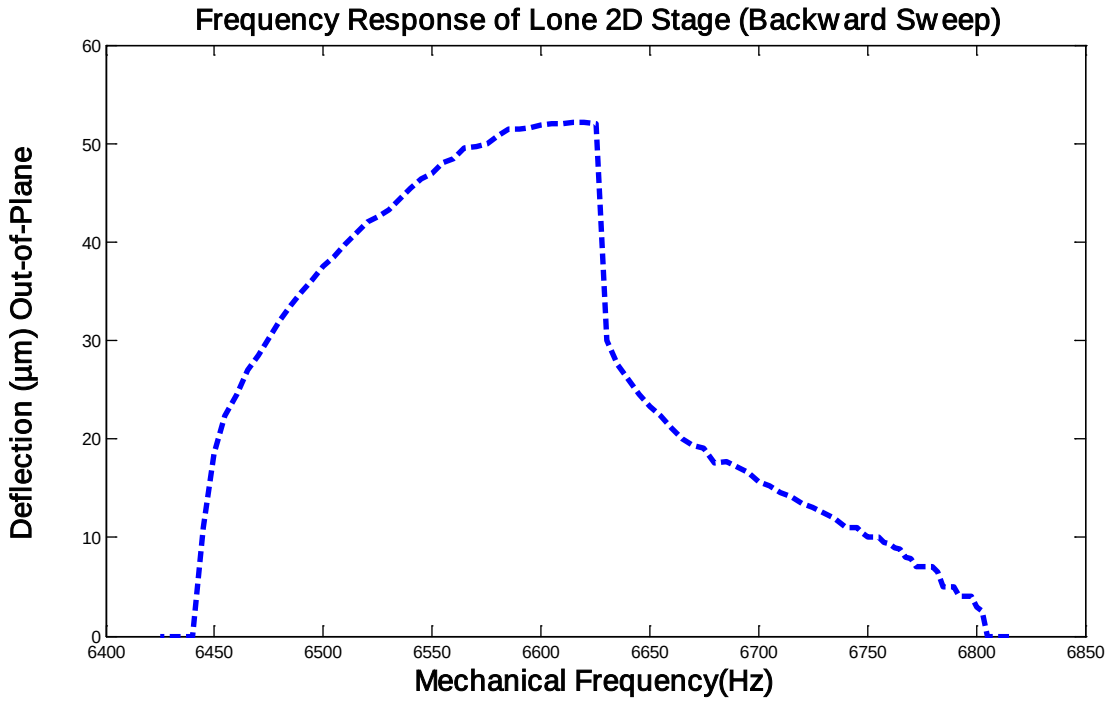

Figure 3.13: Frequency response of 2D MEMS stage without MLA (backward sweep) with applied voltage of 172 Volt peak-to-peak

As described previously, the peak deflection values for backward and forward sweeps are approximately same, but at forward sweep the same amount of deflection is achieved with a lower voltage. The device with MLA and without MLA shows a behavior of an ordinary 2nd order system, this behavior can be observed in the frequency sweeps for both cases. This also indicates that there is a spring stiffening effect instead of electrostatic spring softening which is typical of electrostatic scanners [11, 41]. For bending motion, the resonance frequency increases with vibration amplitude so with excitation voltage [42]. Out-of-plane deflections as a function of applied voltage and resonance frequency change

as a function of applied voltage are given in Figure 3.14 and Figure 3.15 respectively. As can be seen in Figure 3.14, the rate of change of deflection decreases with the increased voltage, which is also an evidence of spring stiffening effect. With the stage, 100 µm peak-to-peak deflection is achieved with an applied voltage of 200 Volt peak-to-peak. Measured frequencies are around 6750 Hz and increase as applied voltage increases. Expected frequency for out-of-plane resonance is approximately 5956 Hz, see Table 3.1, and the measured resonance frequency is close to the expected frequency but a little bit higher than expected. This is due to the fact that the width of springs of released devices is wider than the one used for FEM analysis.

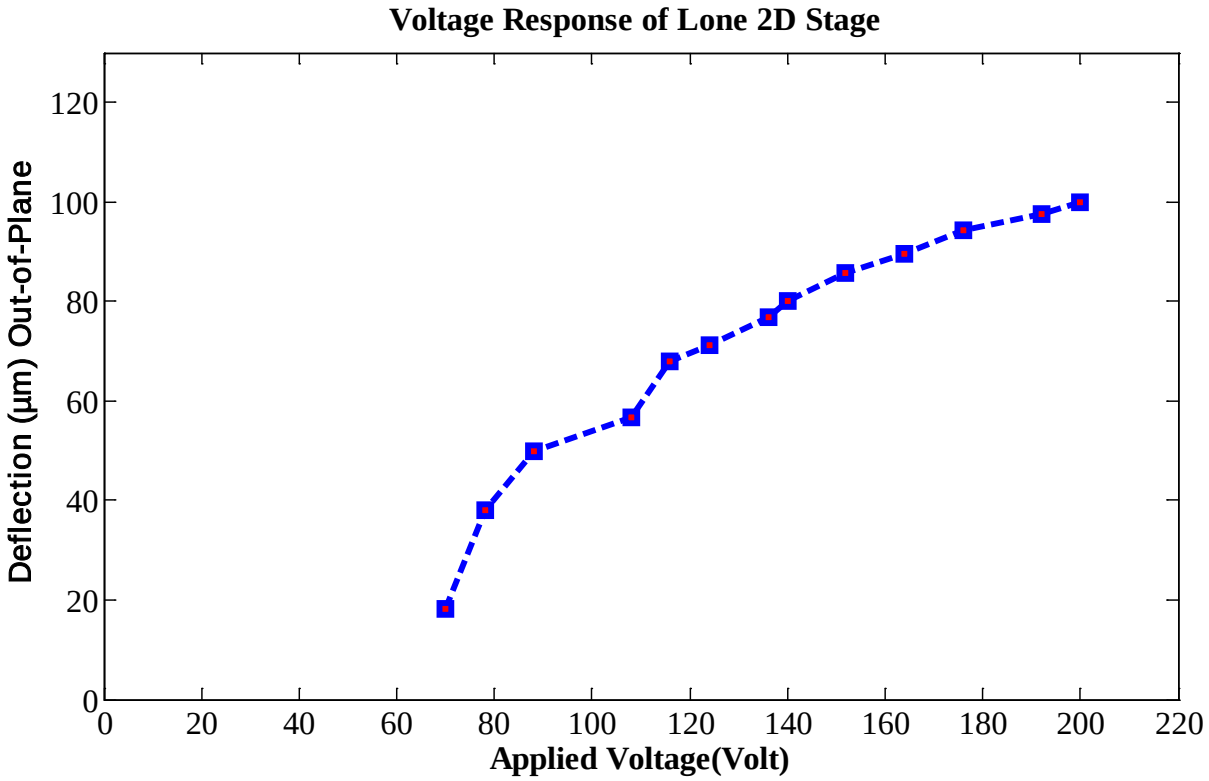

Figure 3.14: Voltage response of 2D MEMS stage without MLA for out-of-plane translation

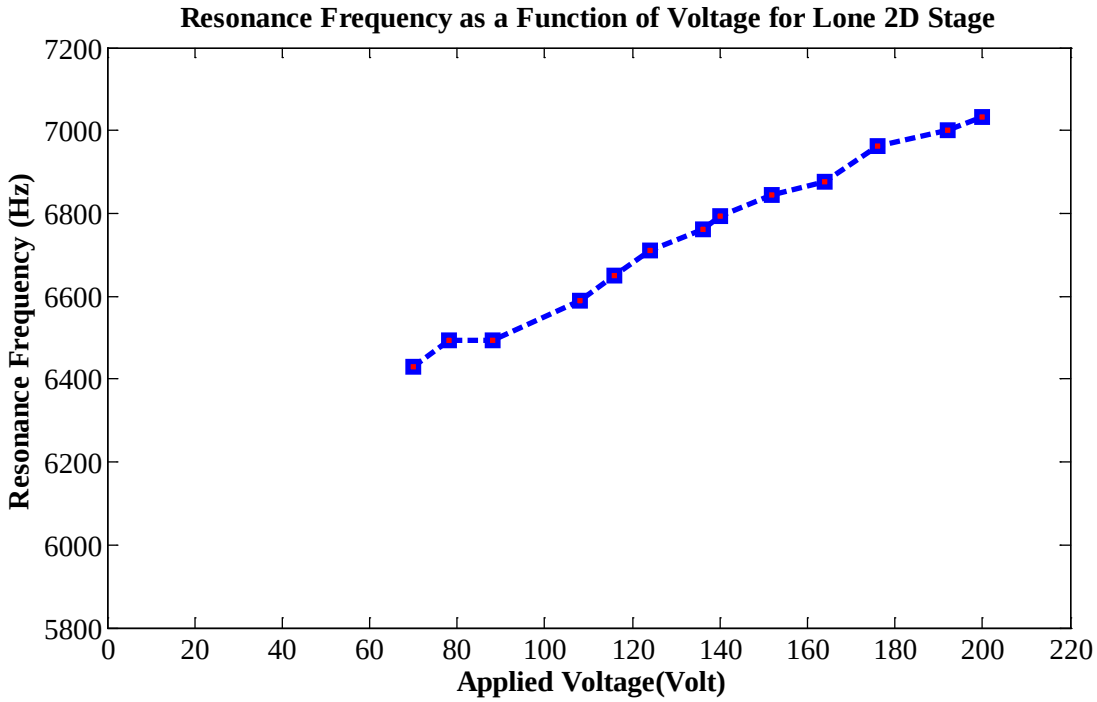

Figure 3.15: Resonance frequency change as a function of applied voltage

Similar measurements were also pursued MLA integrated devices. For the MLA mounted device a deflection 124 μm peak-to-peak at 4193 Hz using 100 V peak-to-peak was achieved. The up- and the down-sweep for the out-of-plane actuation of this device are also given in Figure 3.16. This frequency sweep was obtained with applied voltage of 112 V peak-to-peak. The zig-zag patterns in the frequency response are due to mode coupling around those frequencies, see Figure 3.16. The asymmetry is due to spring stiffening effect and the effect of spring stiffening is more significant for larger deflections.

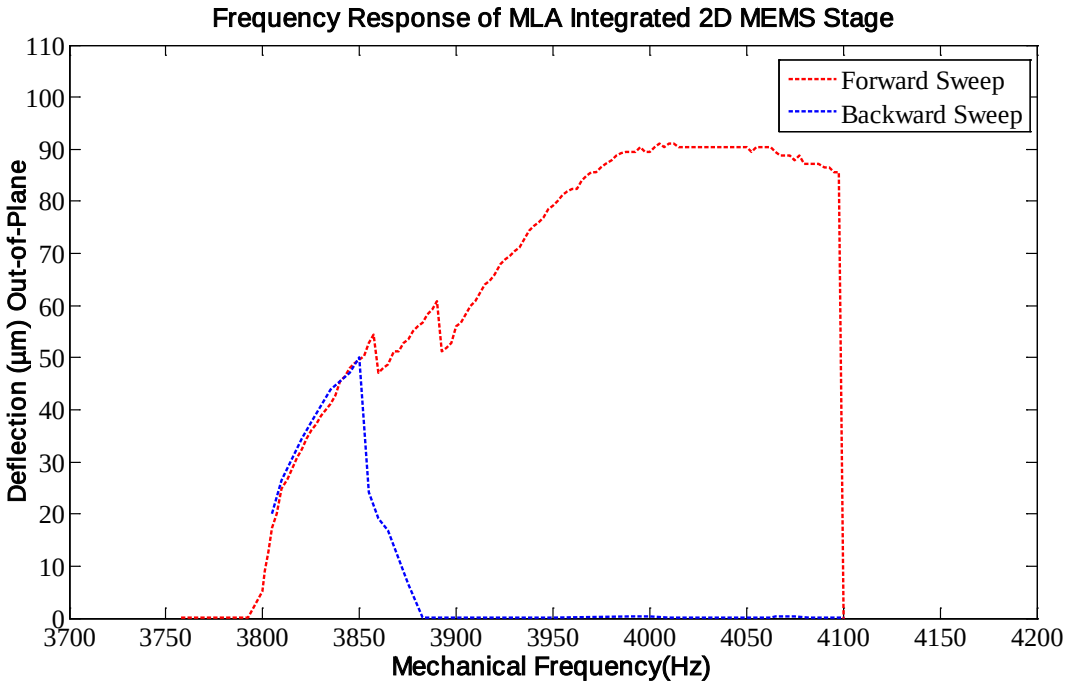

Figure 3.16: Frequency response of MLA integrated 2D MEMS stage for out-of-plane motion

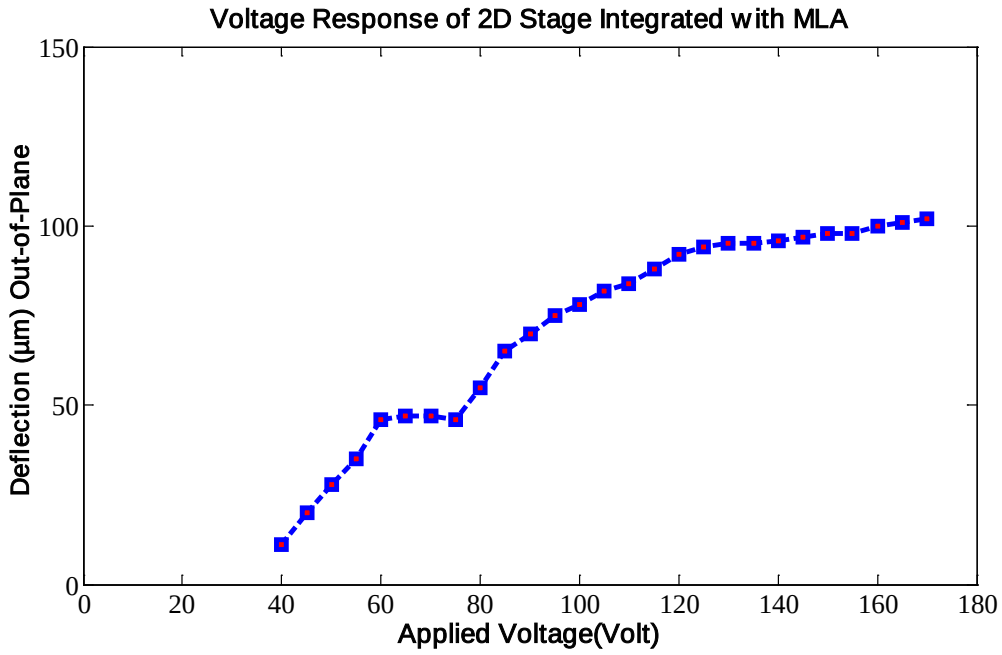

Figure 3.17: Voltage Response of MLA integrated 2D MEMS stage for out-of-plane actuation

Figure 3.17 shows voltage response characteristics of the 2D MEMS stage with MLA, for the out-of-plane mode, a deflection of 102 µm at 4606 Hz using 170 V was achieved. On another sample 124 µm deflection was measured using only 100 V peak-to-peak at 4193 Hz. There are two concerns to be taken into account when comprehending these differences between the performance of different samples. Firstly, the electrical conductivity for different wafers shows diversity, which also affects electro mechanical characteristics of the device. Secondly, the placement of MLA shows difference for different mountings, which also affects the maximum amount of deflections that can be obtained for out-of-plane motion. When looked into the Figure 3.17, the MLA integrated stage shows an asymmetry, which is also due to spring stiffening effect as well, witnessed in only actuator case.

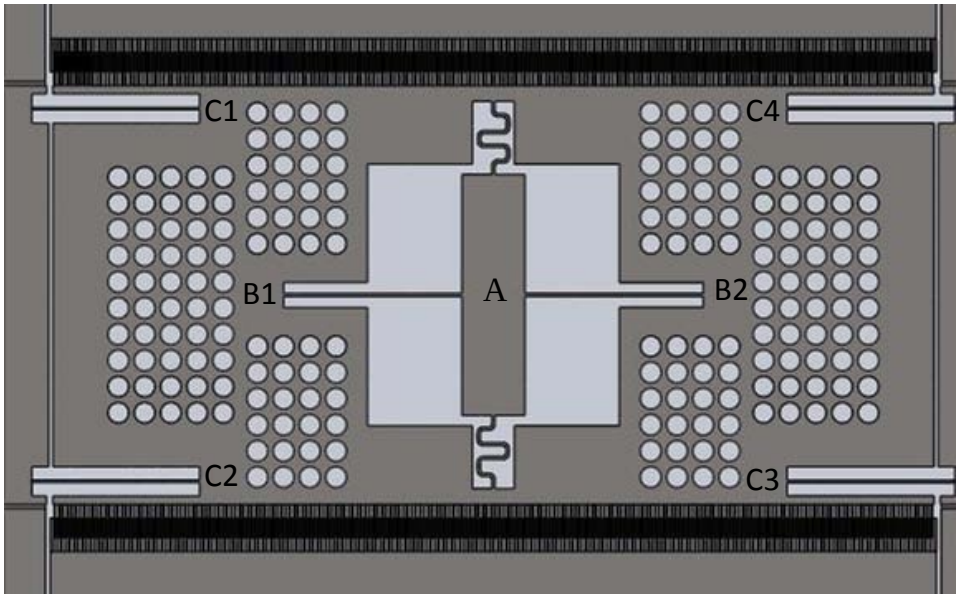

Figure 3.18: Front side view of the device to show deflection distribution for out-of-plane actuation on different locations of the device

Node Name	Deflection for without MLA device (µm)	Deflection for with MLA device (µm)
A	47,2	47,0
B1	37,0	29,4
B2	36,5	29,6
C1	27	22
C2	31	21,6
C3	31,6	21,4
C4	27	22,5

Table 3.3: The amount of deflections for corresponding points illustrated in Figure 3.18

For the second mode of the device (out-of-plane bending), the amount of deflection shows a variety on different portions of the device. Figure 3.18 shows the general top view of the device and 7 points on the wafer and Table 3.3 gives amount of deflections for these points with an applied voltage of 138 V peak-to-peak for both device without MLA and MLA integrated device. For both cases (device with and without MLA), the peak deflections occur around in the middle of inner frame, and the amount of deflections tend to decrease around the spring connection points (C1,C2,C3,C4). The amount of deflection on the upper flexure connection points (C1,C4) are a little bit lower than the upper ones (C2,C3), this unexpected difference stems from the electrical conductivity and electrical connection difference of two sides of the device. The voltages are applied through metal pads, which are defined in the first lithography step; the surface quality of each pad can show differences. These differences lead to unbalanced forces exerted on different sides if the actuator.

3.5.2 In-Plane Actuation

For characterization of the in-plane movement camera output is used to quantify the movement, while LDV used at a tilted angle is utilized to determine the actual oscillation frequency of the stages. For the mounted device 34 μm peak-to-peak deflection of in-plane motion is obtained at the resonance of 1950Hz with 57V peak-to-peak. As described earlier, off-resonance actuation was pursued for the device with and without MLA, sees Figure 3.19 and Figure 3.20. The voltage configuration for in-plane actuation is given as:

$$V_1 = V_{DC} + V_{AC}\sin(wt) \quad (3.1)$$

$$V_2 = V_{DC} - V_{AC}\sin(wt) \quad (3.2)$$

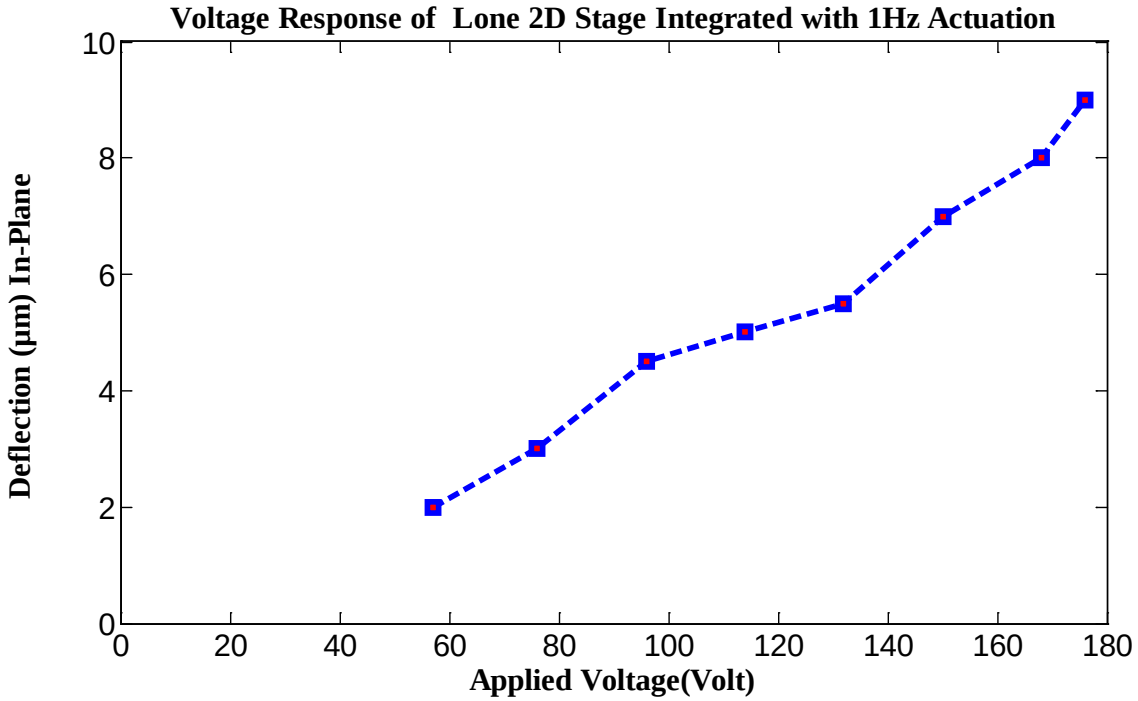

Figure 3.19: Voltage response of 2D MEMS stage without MLA for in-plane actuation with 1Hz

For off-resonance actuations similar voltage responses were observed for both MLA integrated device and stage without MLA. For the in-plane actuation at DC for the device with MLA, 10 μm is achieved at 192 V peak-to-peak and for the stage without MLA, 9 μm is achieved at 178 V peak-to-peak.

The frequency sweep for the device with MLA in-plane motion is given in Figure 3.21. The characterization of in-plane deflections via using camera output comes with a challenge of determining small changes in the deflections with the change of applied voltage or actuation frequency. So, the plateaus in Figure 3.21 could be related to this lack of accurate determination of small changes via camera.

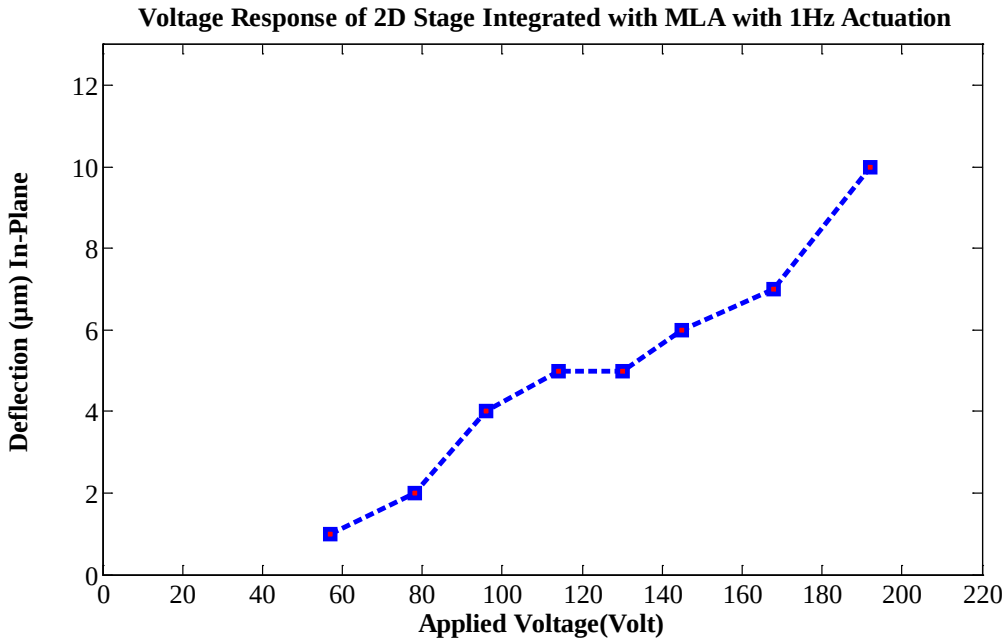

Figure 3.20: Voltage response of MLA integrated 2D stage for in-plane actuation with 1Hz Actuation

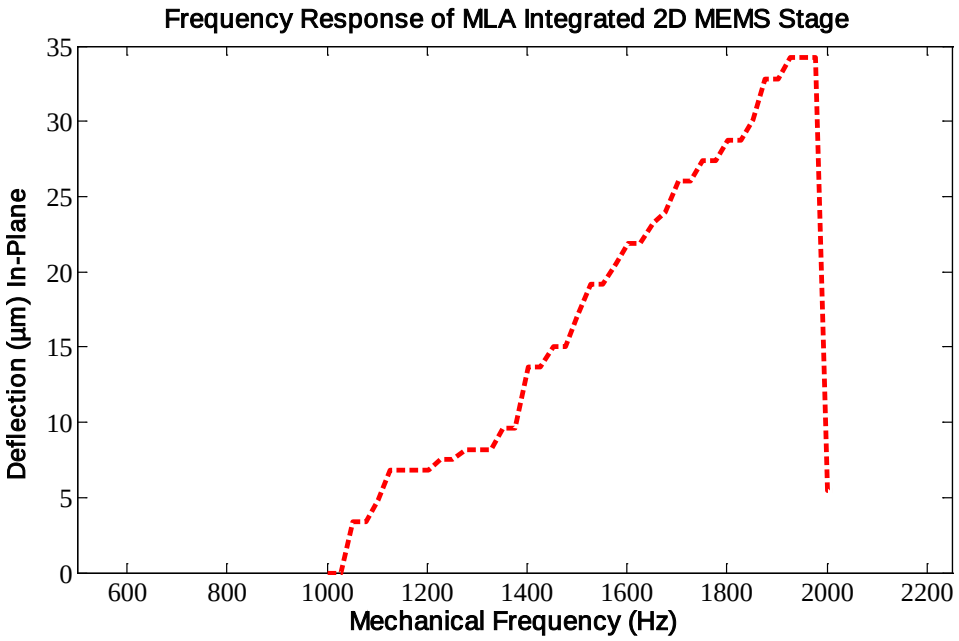

Figure 3.21: Frequency response of MLA integrated 2D MEMS stage for in-plane motion

3.6 Beam Steering Demonstration

As described in the first chapter, the beam steering with cascaded MLA integrated MEMS stages is promising for miniaturized imaging systems. Differently from system described in page 11, two single MLAs were used for steering. An MLA based refractive beam scanner consisting of two MLA integrated on MEMS stage separated by a distance of two focal lengths is shown in Figure 3.22. In this system, the incident collimated beam is separated into several bundles, and each bundle is focused onto an intermediate image plane by the lenslets in the 1st MLA. The 2nd MLA recollimates these bundles and reconstructs the incoming beam. Angular steering of the beam is accomplished by the

lateral translation of the MLAs relative to each other. The details of the beam steering were described in the first chapter.

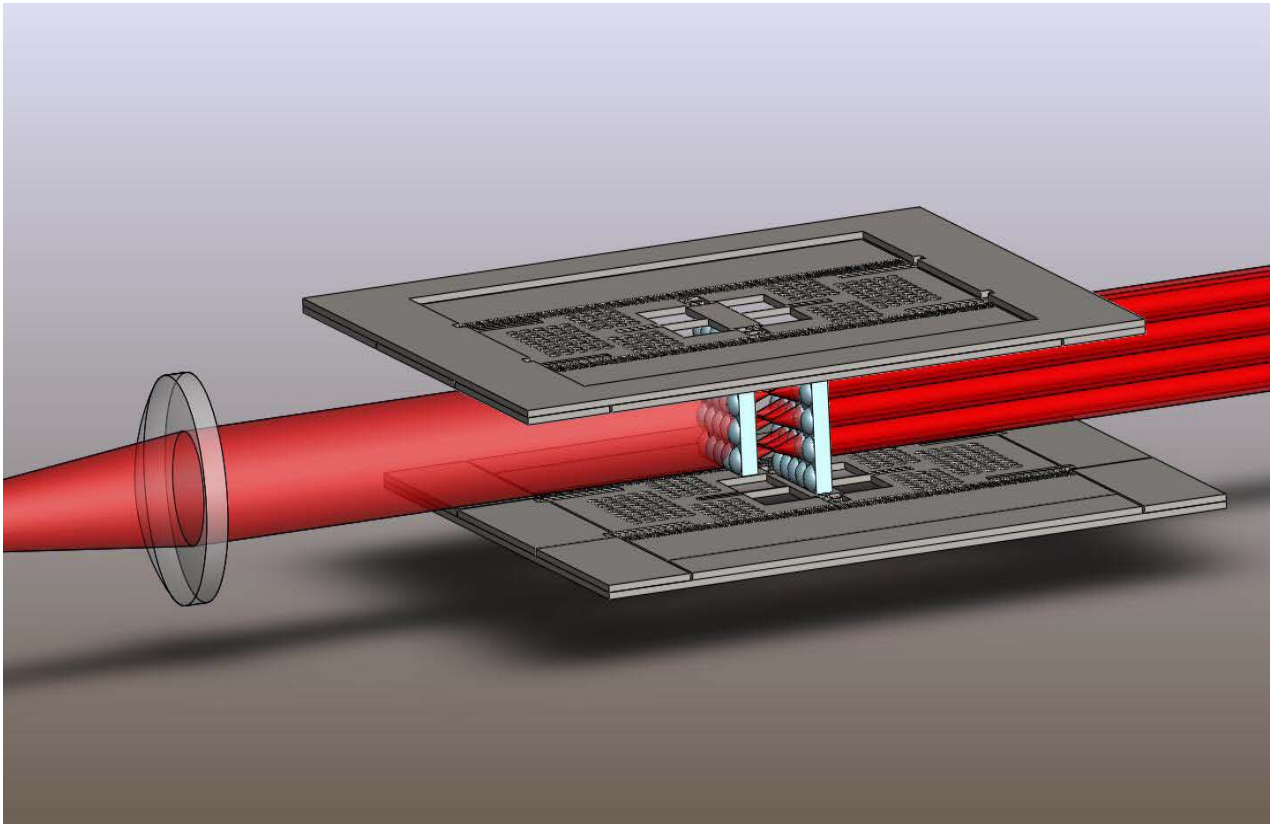

Figure 3.22: Beam steering with two cascaded MLA integrated MEMS stages.

For the sake of simpler optical alignment, only one MLA integrated MEMS stage is used and secondary MLA is a bigger and stationary MLA, see Figure 3.23. The figure show a close-up view of MLA integrated MEMS stage cascaded with a bigger stationary MLA placed on a printed circuit board (PCB) plate.

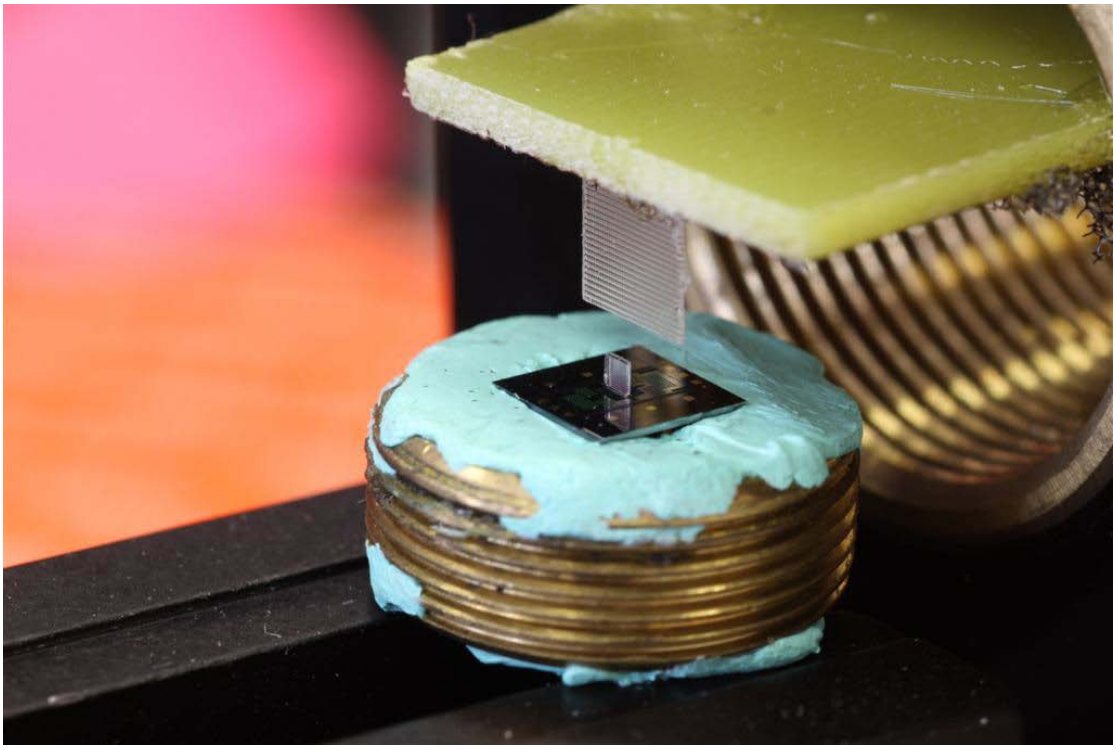

Figure 3.23: MLA integrated MEMS stage cascaded with stationary MLA

When the stage is vibrating a laser beam can be scanned. The resulting scanline achieved by the out-of-plane actuation of the device can be seen in Figure 3.24.

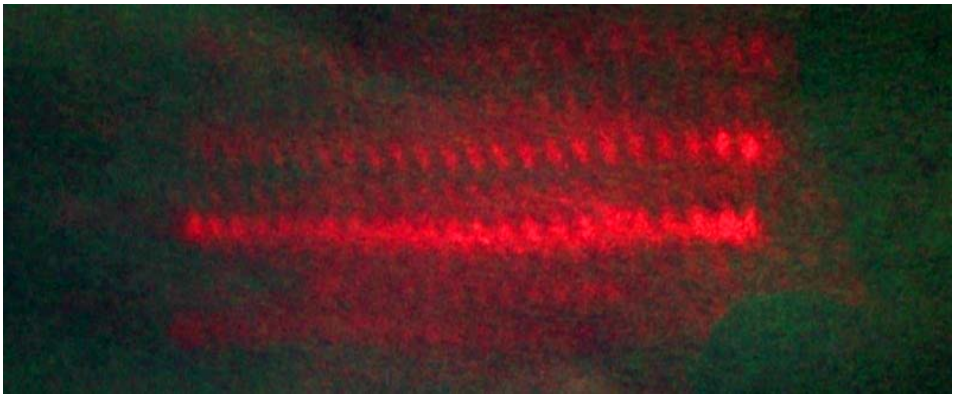

Figure 3.24: A scanline achieved by in-plane motion of the stage

Chapter 4

4 High Frequency Torsional Scanner

Light scanning is used in many applications including , but not limited to, imaging [43], display [35], barcode scanning [44]. MEMS scanners can meet high frequency and low power consumption requirements and they are suitable for miniaturization of these high demanding applications. As described in the first chapter of the thesis, different actuation mechanisms are used for the MEMS scanners, two of the most common actuation mechanisms used for MEMS scanners are electromagnetic and electrostatic actuation.

EM (ElectroMagneticaly) actuated MEMS scanners have already been commercialized for picoprojector applications. EM–actuated scanners can meet high torque requirements but there is a drawback for EM-actuated scanners. They need extra volume for permanent magnet and precise alignment of the permanent magnet. Electrostatic (ES) scanners have fairly simpler fabrication and arrangement of the actuator. ES scanners have been reported by several research groups, [35-36, 45-49].

In this chapter, a novel ES MEMS scanner will be presented. Firstly, a general description of the geometry of the scanner and FEM analysis will be given. Then, the experimental results obtained in ambient and vacuum operation will be given. And the chapter will be concluded with presenting a comparison chart of the highest performing scanners and the scanner presented in this thesis.

4.1 Device Overview

The scanner consists of three frames. The comb finger actuators are placed on the edges of the outermost frame. The electrostatic force is beared only by outermost frame. And the translation is coupled to the inner frame with a mechanical coupling factor,

mechanical coupling principle has been used in the literature [11, 35, 47, 50]. The schematic drawing of the torsional scanner is given in Figure 4.1.

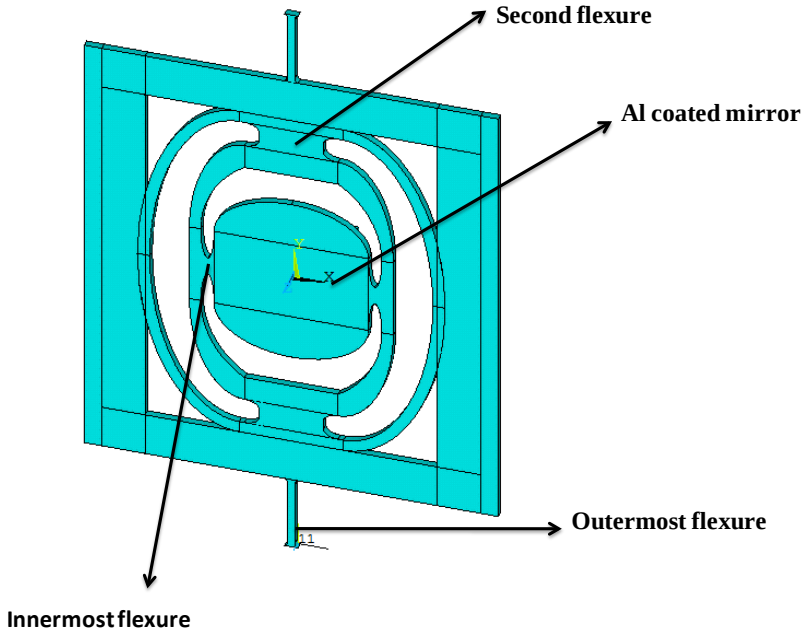

Figure 4.1: The schematic drawing of the torsional scanner

The mirror is aluminum coated and has dimensions of 1.66 mm x 1.5 mm. The mirror constitutes the innermost frame and it is connected to the second frame via the springs that are shown as innermost flexure in the figure. The connection between second frame and outermost frame is executed by second flexures. The whole scanner is connected to the substrate via outermost flexures. The outermost frame that contains the comb finger actuators carries out the actuation. Similar to the 2D actuator described in the previous chapter, this scanner utilizes also uniaxial comb finger for torsional translation. Similar type of actuators used for torsional scanners could be found in the literature [36, 50].

Multi-frame geometry is designed for two main goals. One of the goals is to reduce air damping during high velocity mirror translations by utilizing mechanical coupling principle. The advantage of multi-frame geometry over the ones without extra frame was verified by experimental results in [51]. Second aim for utilizing this multi-frame geometry is to decrease dynamic deformation by increasing the isolation between comb finger actuators and mirror plate.

4.2 Analytical Formulation

The two degree-of-freedom scanner is modeled using the Euler-Lagrange method, where potential and kinetic energies for each component in the system are inspected [52]. For the system sketched in Figure 4.1, θ_i and θ_o represent the mechanical scan angle (MSA) of the inner and outer frame and T_{EXT} is the total electrostatic torque created at the comb-fingers. For this geometry, inner frame is the portion of the scanner that is connected to outer frame via second flexures. In detail, inner frame contains the mirror plate and the elliptical volume that surrounds the mirror plate. The equations of motion of the coupled system are written as:

$$J_i \ddot{\theta}_i + b_i \dot{\theta}_i + k_i(\theta_i - \theta_o) = 0 \tag{4.1}$$

$$J_o \ddot{\theta}_o + b_o \dot{\theta}_o + (k_i + k_o)\theta_o = T_{EXT} + k_i\theta_i \tag{4.2}$$

where J is the inertia, k is the spring constant and b is the damping coefficient. The damping coefficient and spring constant parameters are assumed time independent in the analytical analysis of the system. The subscripts '*i*' and '*o*' denote the inner and the outer frames, respectively.

Unlike single frame scanners in which generally comb actuators are in direct contact with mirror plate, there are two torsion modes of interest in the two-frame scanners: one being out-of-phase (referred to as OP throughout the thesis) and the other one being in-phase (referred to as IP throughout the thesis) with respect to the two frames. In the scanner presented here the inner frame has no direct contact with actuators and a small movement of the outer frame is coupled into and amplified at the inner frame with a mechanical coupling gain (*M*). Figure 4.2 illustrates the frequency response of the mechanically coupled systems with both magnitude and phase information. At the lower vibration frequency, the inner and outer frames move in-phase, whereas at the higher vibration frequency, the frames move out- of- phase [35].

Large mechanical coupling gain can be obtained either at the IP-resonant mode or the OP-resonant mode (as in Figure 4.2) depending on the inertia and the spring constant of the inner and outer frames and flexures. Note that the largest mechanical gain is obtained in between the two resonant modes where the outer frame has a dip. Unfortunately, the deflection of the outer frame is small and that is not an optimum operating point.

The IP- and OP- resonance frequencies of the system are solved and represented by ω_{IP} and $\omega_{OP.}$

$$\omega_{IP}{}^2 = \frac{k_i}{2J_o} + \frac{\omega_o{}^2}{2} + \frac{\omega_i^2}{2} - \Delta \tag{4.3}$$

$$\omega_{OP}{}^2 = \frac{k_i}{2J_o} + \frac{\omega_o{}^2}{2} + \frac{\omega_i^2}{2} + \Delta \tag{4.4}$$

where

$$\Delta = \frac{\sqrt{-4k_i k_o J_i J_o + (k_o J_i + k_i J_i + k_i J_o)^2}}{2J_i J_o} \tag{4.5}$$

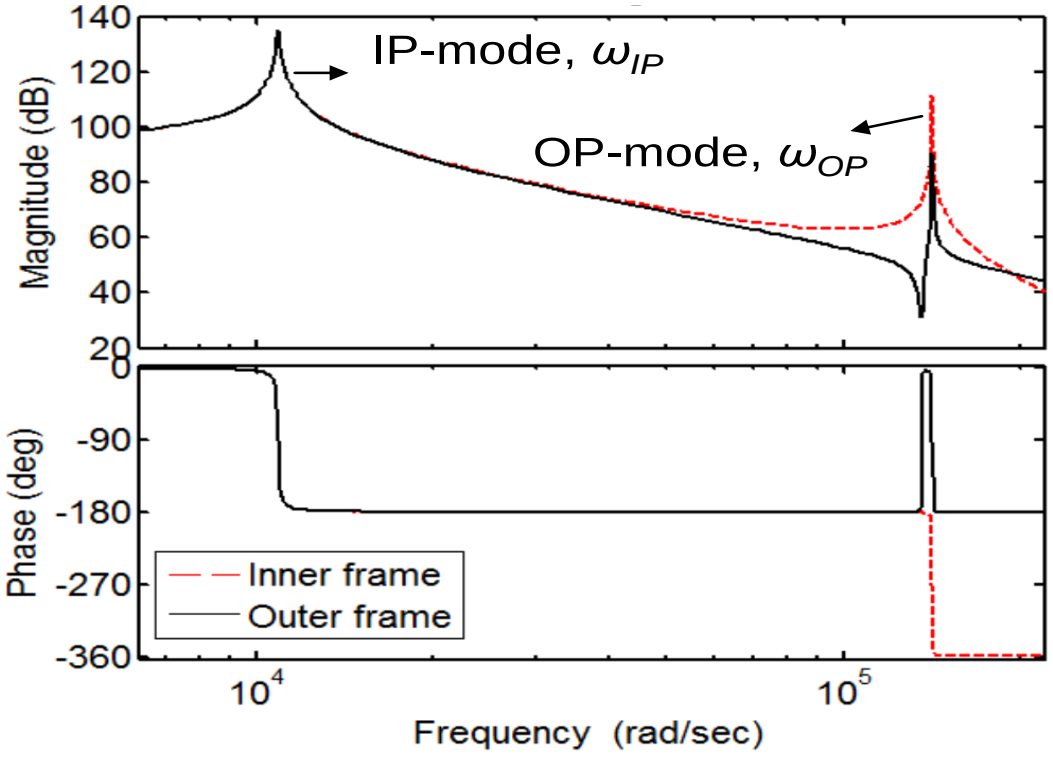

Figure 4.2: Frequency and phase response of the coupled resonator system for two-frame systems [35].

The outer and inner frame rotational deflections can be solved in the Laplace domain for 2-DoF system.

$$J_o\Theta_o(s)s^2 + b_o\Theta_o(s)s + k_i(\Theta_o(s) - \Theta_i(s)) + k_o\Theta_0(s) = T_{EXT} \qquad (4.6)$$

$$J_i\Theta_i(s)s^2 + b_i\Theta_i(s)s + k_i(\Theta_i(s) - \Theta_o(s)) = 0 \tag{4.7}$$

The transfer functions of the coupled system are expressed as:

$$\frac{\Theta_o(s)}{T_{EXT}} = \frac{J_i s^2 + b_i s + k_i}{((J_o s^2 + b_o s + k_i + k_o)(J_i s^2 + b_i s + k_i) - k_i^2)} \tag{4.8}$$

$$\frac{\Theta_i(s)}{T_{EXT}} = \frac{k_i}{((J_o s^2 + b_o s + k_i + k_o)(J_i s^2 + b_i s + k_i) - k_i^2)} \tag{4.9}$$

Setting $s=j\omega$ for steady-state frequency domain analysis, the frequency dependent mechanical coupling gain M is calculated by using (4.8) and (4.9) and shown as:

$$M(\omega) = \left|\frac{\Theta_i(\omega)}{\Theta_o(\omega)}\right| = \frac{k_i}{\sqrt{(k_i - J_i\omega^2)^2 + (b_i\omega)^2}}, \tag{4.10}$$

The analytical calculations by the light of these equations were pursued for the scanner of interest, the analytical results showing ω_{IP} and ω_{OP} are given in Figure 4.4. The ω_{IP} is found to be 2.11 KHz where ω_{OP} is found 28.161KHz. FEM results , which are given in Figure 4.3, give close results to the results obtained from analytical calculations. In FEM results, the corresponding modes are found to be 2.544 KHz (In-phase torsion mode) and 27.986 KHz (Out-of-phase torsion mode).

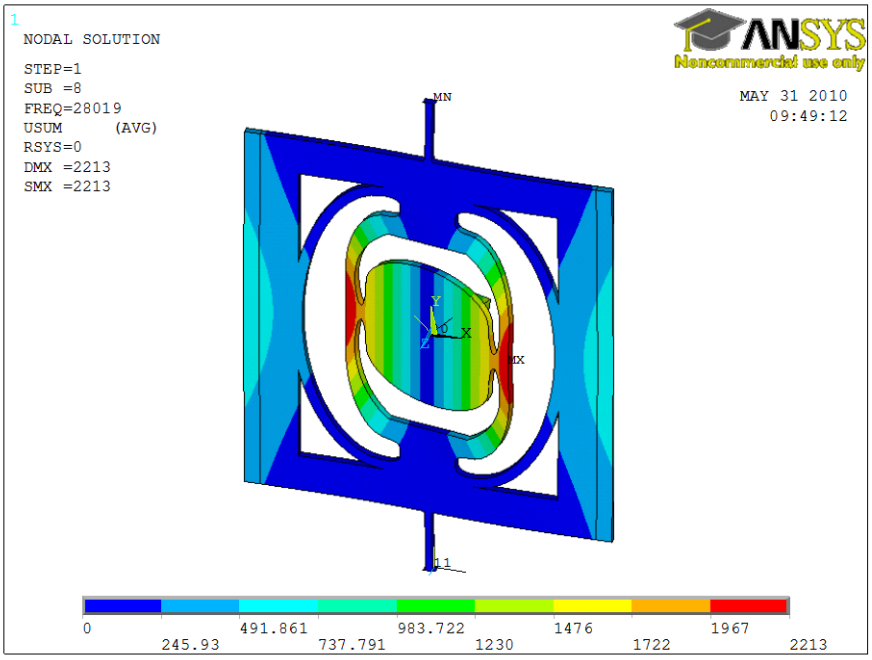

Figure 4.3: The out-of-phase torsional mode of the torsional scanner

The presented device is designed to achieve 56 º Total Optical Scan Angle (TOSA) at its coupling frequency and the parameters are adjusted to keep the maximum stress below 1.5 GPa for the required mechanical deflection. Different design iterations were pursued to achieve this amount of deflection under maximum stress level, and the minimum stress value achieved for desired TOSA value is 1.74 GPa.

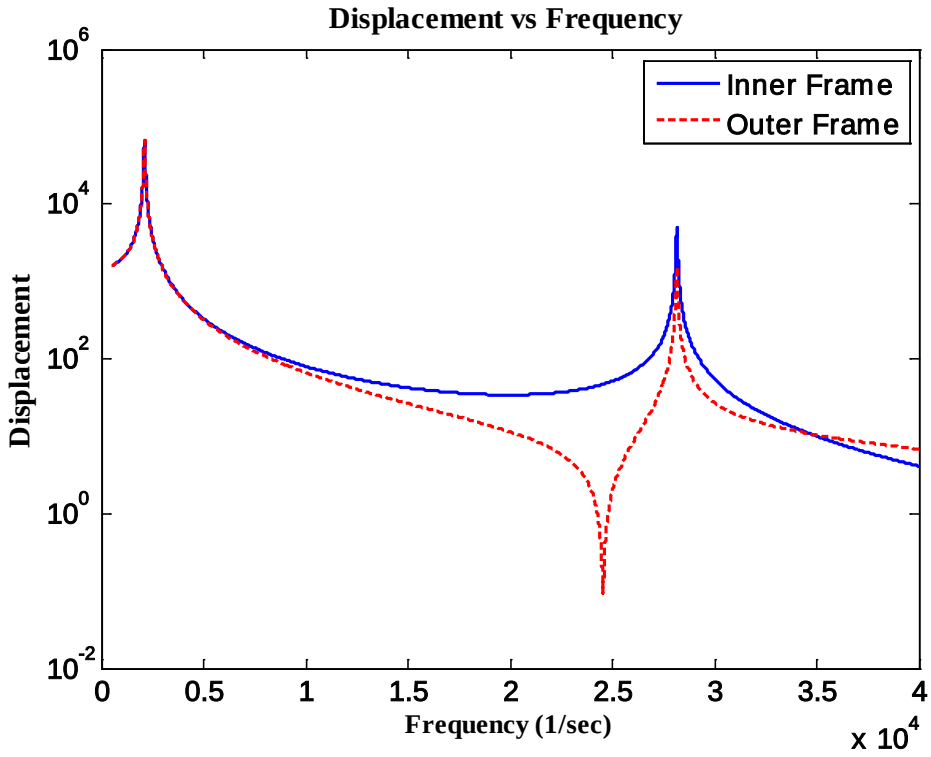

Figure 4.4: Analytical results showing frequency versus displacement

4.3 Microfabrication

The microfabrication of the torsional scanners is similar to the microfabrication of 2D MEMS stages. Devices were fabricated on Silicon-On-Isolator (SOI) wafers with a 240 µm thick handle layer, a 2 µm thick buried oxide (BOX) and a 75 µm device layer, the latter determining the thickness of the entire mechanical structure. The three mask fabrication process is shown in Fig. 3 and Fig. 4. As starting material silicon-on-insulator (SOI) wafers with a doped 75 µm thick device layer are used (Figure 4.5a). To form the wire-bond electrodes and the mirror coating, Al is sputtered onto the device layer (Figure 4.5b) and then patterned by photolithography using mask 1 (Figure 4.5c). Next, the device structures

are defined through lithography with mask 2 and front side deep reactive ion etch (DRIE) (Figure 4.5d). Mask 3 is now used to perform lithography for backside windowing. After the backside DRIE (Figure 4.5e) the devices are released through etch of the buried oxide in HF vapor (Figure 4.5f).

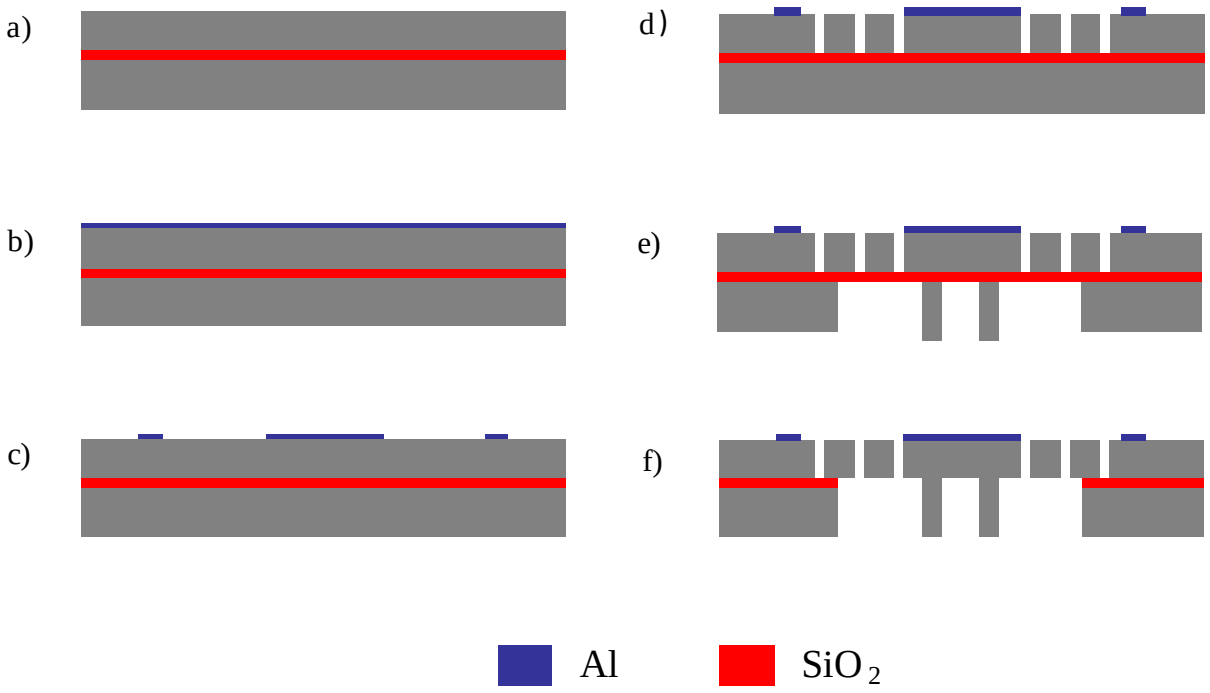

Figure 4.5: The process flow of torsional scanner

SEM picture showing a general top view of the scanner is given in Figure 4.5.

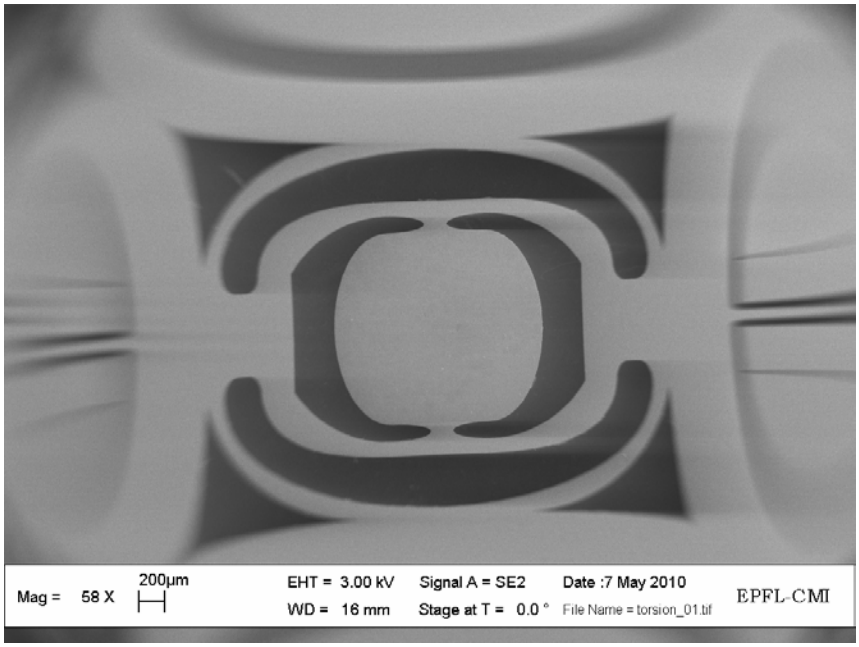

Figure 4.6: SEM picture showing front side of the torsional scanner

4.4 Experimental Results

The dynamic behavior of the comb-drive scanner varies with the excitation signal and can be modeled with the second-order differential equation given by equations in (4.1) and (4.2). At the torsional mode, the capacitance varies with the angular deflection and the electrostatic torque depends on the displacement as well as the excitation voltage [37]. The created torque's dependence on deflection creates momentarily change on torsional stiffness and the system is defined by parametric nonlinear ordinary differential equations. Similar to the out-of-plane motion of the 2D stages, there are two jump frequencies ($f_1$and f_2). In this part, the experimental results showing voltage and frequency response of the torsional scanner will be presented. During experiments, two different devices are used.

These devices are selected from two different wafers; the devices will be called as Device 1 and Device 2 hereafter. Experiments were carried out both in ambient and vacuum. This signal is applied to comb-fingers placed on either side of the outer frame. In order to achieve the maximum angular rotation, the excitation signal is applied at frequencies equal to two times of out-of-phase resonance frequencies of the torsional mode. The voltage configuration for torsional actuation is given as:

$$V_1 = V_{DC} + V_{AC}\sin(wt) \quad (4.1)$$

$$V_2 = V_{DC} + V_{AC}\sin(wt) \quad (4.2)$$

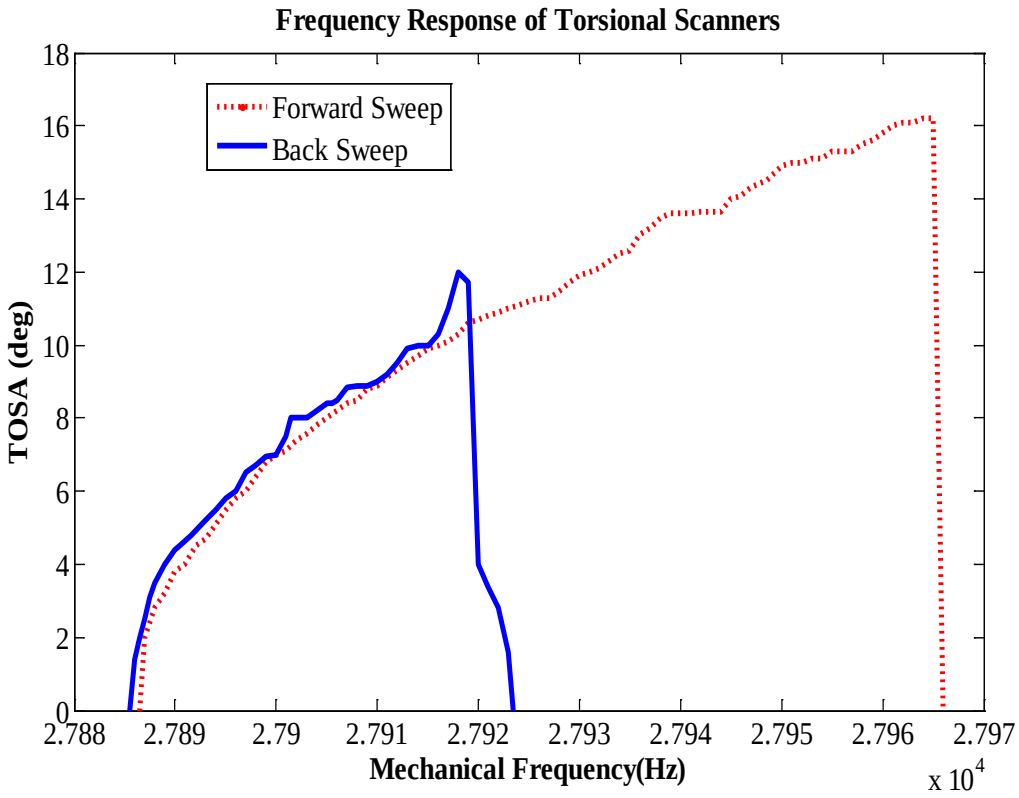

Figure 4.7: Frequency response of torsional scanners for out-of-phase torsional mode

Figure 4.7 shows the frequency response of the Device 2, the sweep was obtained with an applied voltage of 200 Volt peak-to-peak. The maximum achieved scan angles were observed during forward sweep, which is due to spring stiffening effect, this behavior of the scanner is different from the electrostatic scanners presented in the literature [35, 49-50]. The maximum TOSA achieved with 200 Volt peak-to-peak is 16.2 º in the forward sweep at mechanical frequency of 27965 Hz, where TOSA of 12 º is achieved during backward sweep mechanical frequency of 27918 Hz.

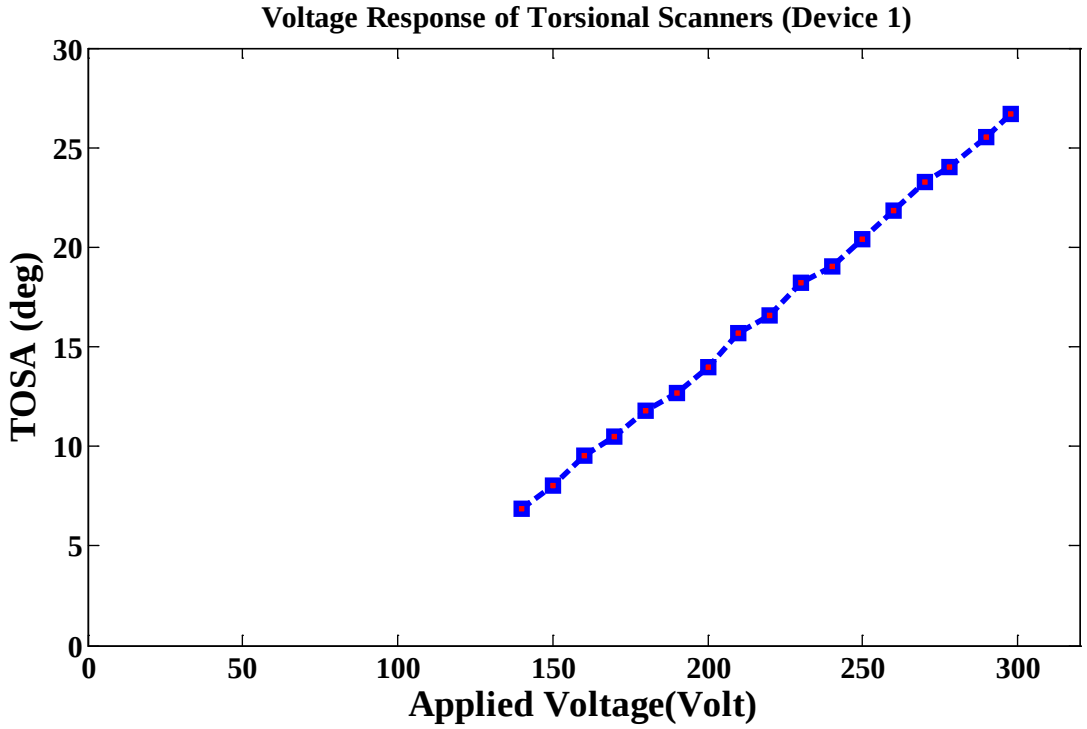

Figure 4.8: Voltage response of torsional scanners at out-of-phase torsional mode (Device 1)

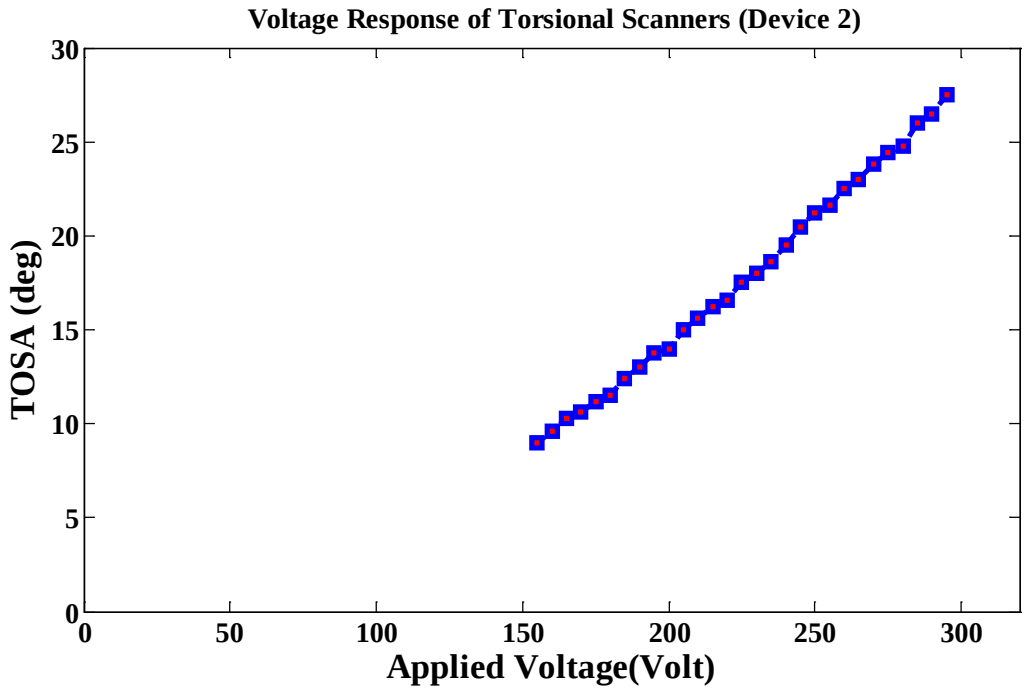

Figure 4.9: Voltage response of torsional scanners at out-of-phase torsional mode (Device 2)

The voltage response, showing obtained maximum TOSA for different excitation voltage for Device 1 and Device 2, are given in Figure 4.8 and Figure 4.9 respectively. As discussed previously, the maximum scan angle is obtain7ed during the forward sweep frequency and the corresponding TOSA values are plotted in Figure 4.8 and Figure 4.9. The voltages of the devices that start oscillation are around 150 Volt peak-to-peak. The voltage response characteristics are also investigated in the low pressure condition, see Figure 4.10. In vacuum, the oscillations start around 42 Volt peak-to-peak and maximum TOSA achieved is 36.18º with an applied voltage of 113 Volt peak-to-peak. After this point, the devices are broken. Spring stiffening effect can be observed also in Figure 4.10, the rate of change of the displacement starts to decrease after large deflections.

Voltage stability of Device 2 is given in Figure 4.11. With an applied voltage of 298 Volt peak-to-peak, 26.7º TOSA is obtained at 28417 Hz with Device 1, and achieved scanline with the probed device is shown in Figure 4.13. The maximum TOSA for Device 2 is 27.5 º at mechanical frequency of 28061 Hz.

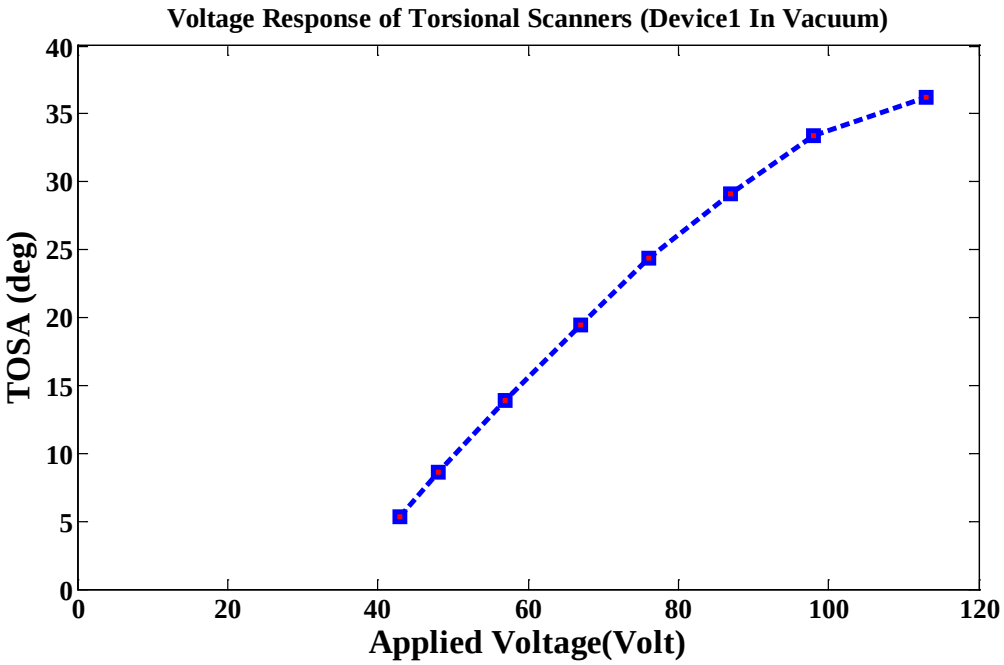

Figure 4.10: Voltage response of torsional scanners at out-of-phase torsional mode in vacuum (Device 1)

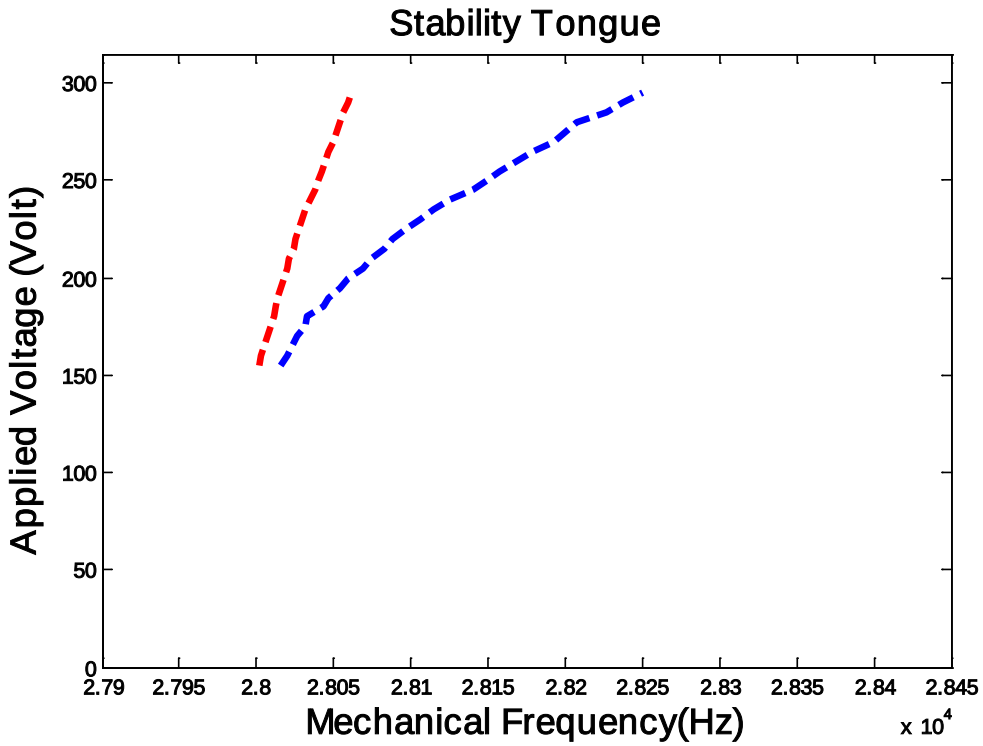

Figure 4.11: Voltage stability curve of Device 2

For evaluation of the performance of this torsional scanner, a comparison chart is given in Figure 4.11 . The figure compares the published scanners in terms of their performances. The figure of merit to evaluate the scanner performance is chosen as $\theta_{OPT} \cdot D$-product, where θ_{OPT} and D refers to TOSA and mirror size respectively. The scanner reported in this paper, marked as "1" in the figures, is close to the highest performing devices in the literature and exceeds the frequency and scan-angle mirror-size requirements of SVGA and HDTV display systems. It should be noted that the highest performance of the scanner is taken into account for this comparison chart, which is obtained in vacuum.

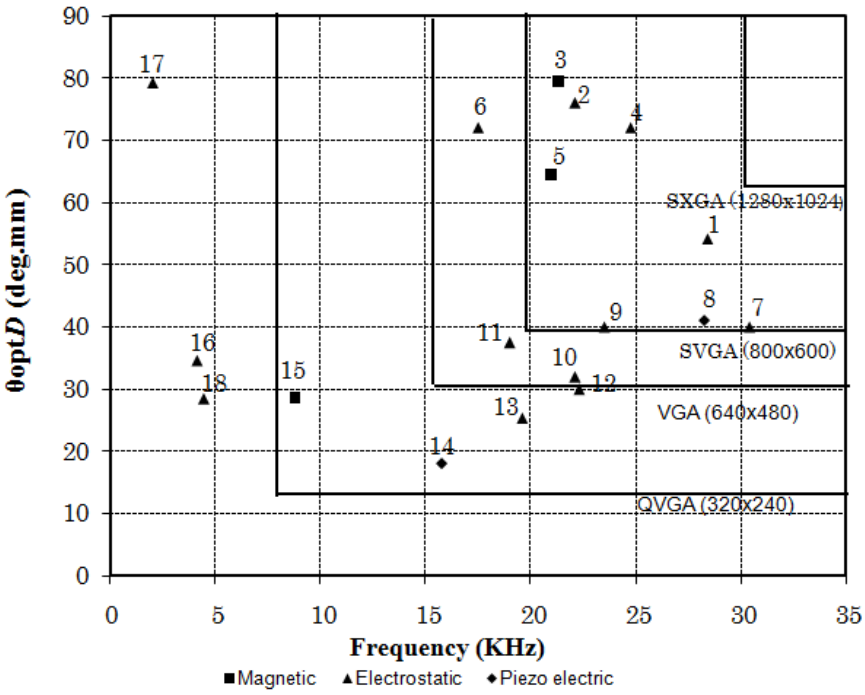

1.This work	6.Urey[7]	11.Wine[53]	16.Kim[45]
2.Arslan [35]	7.Hsu[54]	12.Yoda[46]	17.Il Woong[41]
3.Yalcinkaya[52]	8.Park[55]	13.Ji[56]	18.Milanovic[57]
4. Cho [58]	9. Kuijpers[59]	14.Lebedev[12]	
5.Torashima [60]	10.Ko[61]	15.Ji[8]	

Figure 4.12: Microscanner performance comparison based on the literature. Only high performance scanners are put in the comparison chart.

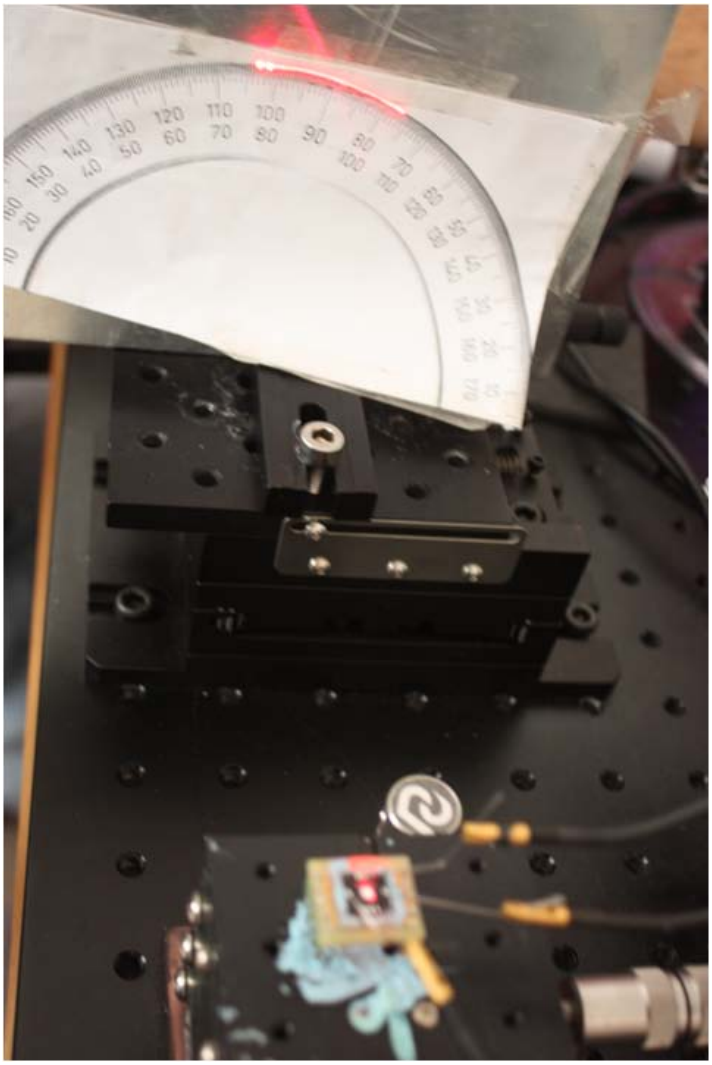

Figure 4.13: The scanline corresponds to 26.7º TOSA at 28417 Hz

Chapter 5

5 Conclusions

In this research progress, two different electrostatically actuated MEMS stages are developed, designed, fabricated and characterized.

One of the designs is 2D MEMS translational stages. These stages are designed for endoscopic laser imaging. One main strong side of these stages is to use uniaxial to deflect along two dimensions. In that sense, in-plane actuation can be observed both in resonance and off resonance where out-of-plane actuation can be observed only in resonance. To achieve desired beam steering, polymer MLAs are hybrid integrated onto MEMS stages. Design effort has taken especially to enhance mode separation between desired modes and the adjacent modes. While arranging mode separation, stress limit of 1.5 GPa is taken into account. The designed 2D MEMS translational stages are fabricated using standard SOI technology. MLAs are integrated after microfabrication of the stages. The characterization of 2D MEMS stages without MLA and MLA integrated 2D MEMS stages are given in this thesis as well. Functional devices integrated MLA are able to deflect 124 μm along out-of-plane and 34 μm along in-plane. Beam demonstration using MLA integrated MEMS stages are demonstrated also in this work.

As a future work, the off-resonance in-plane translation range are planned to enhance. The limitation comes of spring stiffening behavior of the flexures; this can be enhanced using T-bar shape around connection points of the flexures to the scanner area. One of the improvements can be to define a well aligned and sized groove, which is to place MLAs precisely. Manual integration of MLAs, which are carried out using mechanic translational stages , make devices more susceptible to couple to undesired modes and change the mode separation between adjacent modes.

Secondly, a novel high frequency torsional scanner is designed, developed, fabricated and characterized. This high frequency microscanner employs 1.5 x 1.66 mm Al coated mirror plate. The scanner comprises three frames; this multiframe geometry is designed to decrease dynamic deformation by increasing isolation between mirror and comb actuators and to decrease air damping seen by comb fingers by utilizing mechanical coupling principle. The specifications of for this torsional scanner are to obtain 56^{o} TOSA at around 29 KHz with obtaining these specifications not exceeding stress limit. With the fabricated functional devices, TOSA of 26.7^{o} and 36.1^{o} are achieved in ambient and vacuum respectively, oscillation frequencies are for both cases around 28 KHz.

As an improvement of mechanical characteristics of the scanner, the mechanical coupling ratio could be increased with arranging inertia ratio of the frames by taking the mode issue into consideration. And the total capacitances employed for actuation could be increased without changing mode separation so much, to increase the amount of deflection. The stress value for deflection of 56^{o} TOSA is found to be 1.74 GPa during FEM analysis. To decrease this stress value for specified amount of deflection, different spring geometries and fillet shapes around flexures could be tried as a future progress.

BIBLIOGRAPHY

[1] K. E. Petersen, "Silicon as a Mechanical Material," *Proceedings of the Ieee,* vol. 70, pp. 420-457, 1982.

[2] S. Y. Yang and T. Saif, "Mechanical response of single living cells by bio-MEMS sensors," *Mems 2004: 17th Ieee International Conference on Micro Electro Mechanical Systems, Technical Digest,* pp. 265-267
868, 2004.

[3] H. Ra, W. Piyawattanametha, Y. Taguchi, D. Lee, M. J. Mandella, and O. Solgaard, "Two-dimensional MEMS scanner for dual-axes confocal microscopy," *Journal of Microelectromechanical Systems,* vol. 16, pp. 969-976, Aug 2007.

[4] N. A. Hall, B. Bicen, M. K. Jeelani, W. Lee, S. Qureshi, F. L. Degertekin, and M. Okandan, "Micromachined microphones with diffraction-based optical displacement detection," *Journal of the Acoustical Society of America,* vol. 118, pp. 3000-3009, Nov 2005.

[5] H. N. Kwon and J. H. Lee, "A micromachined 2x2 optical switch aligned with bevel-ended fibers for low return loss," *Journal of Microelectromechanical Systems,* vol. 13, pp. 258-263, Apr 2004.

[6] C. H. Chong, K. Isamoto, and H. Toshiyoshi, "Optically modulated MEMS scanning endoscope," *Ieee Photonics Technology Letters,* vol. 18, pp. 133-135, Jan-Feb 2006.

[7] H. Urey, "Torsional MEMS scanner design for high-resolution scanning display systems," Seattle, WA, USA, 2002, pp. 27-37.

[8] C. H. Ji, M. Choi, S. C. Kim, K. C. Song, J. U. Bu, and H. J. Nam, "Electromagnetic two-dimensional scanner using radial magnetic field," *Journal of Microelectromechanical Systems,* vol. 16, pp. 989-996, Aug 2007.

[9] G. D. Gray and P. A. Kohl, "Modeling and performance of a magnetic MEMS wiping actuator," *Microelectromechanical Systems, Journal of,* vol. 15, pp. 904-911, 2006.

[10] S. Kutal Gokce, S. Holmstrom, C. Hibert, C. Ataman, A. Arslan, H. R. Seren, and H. Urey, "MEMS Stage Integrated with Microlens Arrays for High-Resolution Beam Steering," *Procedia Chemistry,* vol. 1, pp. 1319-1322, 2009.

[11] A. Arslan, C. Ataman, S. Holmstrom, K. Hedsten, H. Rahmi Seren, H. Urey, and P. Enoksson, "Mechanically coupled comb drive MEMS stages," in *Optical MEMs*

and Nanophotonics, 2008 IEEE/LEOS Internationall Conference on, 2008, pp. 140-141.

[12] M. Lebedev, H. Sato, and J. Akedo, "Optical micro-scanner fabricated on stainless steel by aerosol deposition method," *2004 14th IEEE International Symposium on Applications of Ferroelectrics-ISAF-04*, pp. 165-168
335, 2004.

[13] M. Kurita, T. Yamazaki, H. Kohira, M. Matsumoto, R. Tsuchiyama, J. U. Xu, T. Harada, Y. Inoue, L. Z. Su, and K. Kato, "An active-head slider with a piezoelectric actuator for controlling flying height," *Ieee Transactions on Magnetics,* vol. 38, pp. 2102-2104, Sep 2002.

[14] J. T. W. Yeow, V. X. D. Yang, A. Chahwan, M. L. Gordon, B. Qi, I. A. Vitkin, B. C. Wilson, and A. A. Goldenberg, "Micromachined 2-D scanner for 3-D optical coherence tomography," *Sensors and Actuators a-Physical,* vol. 117, pp. 331-340, Jan 14 2005.

[15] W. Piyawattanametha and T. D. Wang, "MEMS-Based Dual-Axes Confocal Microendoscopy," *Selected Topics in Quantum Electronics, IEEE Journal of,* vol. PP, pp. 1-11, 2009.

[16] C. P. B. Siu, H. Zeng, and M. Chiao, "Magnetically actuated MEMS microlens scanner for in vivo medical imaging," *Optics Express,* vol. 15, pp. 11154-11166, Sep 3 2007.

[17] C. Chong, K. Isamoto, M. Nakada, H. Fujita, and H. Toshiyoshi, "A Photovoltaically Modulated MEMS Optical Scanner for Fiber Endoscope," in *Microtechnologies in Medicine and Biology, 2006 International Conference on*, 2006, pp. 135-138.

[18] M. Douglass, "DMD reliability: a MEMS success story," 2003, pp. 1-11.

[19] S. Schweizer, P. Cousseau, G. Lammel, S. Calmes, and P. Renaud, "Two-dimensional thermally actuated optical microprojector," *Sensors and Actuators A: Physical,* vol. 85, pp. 424-429, 2000.

[20] T. Yamanoi, T. Endo, and H. Toshiyoshi, "A hybrid-assembled MEMS Fabry-Perot wavelength tunable filter," *Sensors and Actuators a-Physical,* vol. 145, pp. 116-122, Jul-Aug 2008.

[21] C. Antoine, X. Li, J. S. Wang, and O. Solgaard, "Reconfigurable optical wavelength multiplexer using a MEMS tunable blazed grating," *Journal of Lightwave Technology,* vol. 25, pp. 3100-3107, Oct 2007.

[22] J. S. Milne, J. M. Dell, A. J. Keating, and L. Faraone, "Widely Tunable MEMS-Based Fabry-Perot Filter," *Journal of Microelectromechanical Systems,* vol. 18, pp. 905-913, Aug 2009.

[23] C. Lee, "A MEMS VOA using electrothermal actuators," *Journal of Lightwave Technology,* vol. 25, pp. 490-498, Feb 2007.

[24] A. Bashir, P. Katila, N. Ogier, B. Saadany, and D. A. Khalil, "A MEMS-based VOA with very low PDL," *Ieee Photonics Technology Letters,* vol. 16, pp. 1047-1049, Apr 2004.

[25] H. B. Liu and F. Chollet, "Moving Polymer Waveguides and Latching Actuator for 2 x 2 MEMS Optical Switch," *Journal of Microelectromechanical Systems,* vol. 18, pp. 715-724, Jun 2009.

[26] C. H. Ji, Y. Yee, J. Choi, S. H. Kim, and J. U. Bu, "Electromagnetic 2 x 2 MEMS optical switch," *Ieee Journal of Selected Topics in Quantum Electronics,* vol. 10, pp. 545-550, May-Jun 2004.

[27] A. Akatay, C. Ataman, and H. Urey, "High-resolution beam steering using microlens arrays," *Optics Letters,* vol. 31, pp. 2861-2863, Oct 1 2006.

[28] A. Tuantranont, V. M. Bright, J. Zhang, W. Zhang, J. A. Neff, and Y. C. Lee, "Optical beam steering using MEMS-controllable microlens array," *Sensors and Actuators a-Physical,* vol. 91, pp. 363-372, Jul 15 2001.

[29] J. D. Berger, Z. Yongwei, J. D. Grade, H. Lee, S. Hrinya, H. Jerman, A. Fennema, A. Tselikov, and D. Anthon, "Widely tunable external cavity diode laser using a MEMS electrostatic rotary actuator," in *Optical Communication, 2001. ECOC '01. 27th European Conference on*, 2001, pp. 198-199 vol.2.

[30] B. Legrand, A. S. Rollier, L. Buchaillot, and D. Collard, "Parallel Plate Electrostatic Actuators in Liquids: Displacement-Voltage Optimisation for Microfluidic Applications," in *Micro Electro Mechanical Systems, 2006. MEMS 2006 Istanbul. 19th IEEE International Conference on,* 2006, pp. 718-721.

[31] E. Dumsong, N. Afzulpurkar, and A. Tuantranont, "Design, Analytical Modeling, and Simulation of Wire-Free Walking Scratch-Drive Microrobot," *Ieee Transactions on Industrial Electronics,* vol. 56, pp. 1109-1120, Apr 2009.

[32] N. Quack, P. Rüst, S. Blunier, J. Dual, F. Felder, M. Rahim, M. Fill, M. Arnold, and H. Zogg, "A comb drive actuated vertically moving micromirror for tunable mid-infrared Resonant Cavity Enhanced Detectors," *Microelectronic Engineering,* vol. 86, pp. 1243-1246.

[33] P. Srinivasan, C. O. Gollasch, and M. Kraft, "Three dimensional electrostatic actuators for tunable optical micro cavities," *Sensors and Actuators A: Physical,* vol. In Press, Corrected Proof.

[34] E. Bulgan, Y. Kanamori, and K. Hane, "Submicron silicon waveguide optical switch driven by microelectromechanical actuator," *Applied Physics Letters,* vol. 92, pp. -, Mar 10 2008.

[35] A. Arslan, D. Brown, W. O. Davis, S. Holmstrom, S. K. Gokce, and H. Urey, "Comb-Actuated Resonant Torsional Microscanner With Mechanical Amplification," *Microelectromechanical Systems, Journal of,* vol. PP, pp. 1-8, 2010.

[36] H. Schenk, P. Durr, D. Kunze, H. Lakner, and H. Kuck, "A resonantly excited 2D-micro-scanning-mirror with large deflection," *Sensors and Actuators a-Physical,* vol. 89, pp. 104-111, Mar 20 2001.

[37] C. Ataman and H. Urey, "Modeling and characterization of comb-actuated resonant microscanners," *Journal of Micromechanics and Microengineering,* vol. 16, pp. 9-16, Jan 2006.

[38] W. Piyawattanametha, P. R. Patterson, D. Hah, H. Toshiyoshi, and M. C. Wu, "Surface- and bulk-micromachined two-dimensional scanner driven by angular vertical comb actuators," *Journal of Microelectromechanical Systems,* vol. 14, pp. 1329-1338, Dec 2005.

[39] K. L. Turner, S. A. Miller, P. G. Hartwell, N. C. MacDonald, S. H. Strogatz, and S. G. Adams, "Five parametric resonances in a microelectromechanical system," *Nature,* vol. 396, pp. 149-152, 1998.

[40] A. Wolter, H. Schenk, H. Korth, and H. Lakner, "Torsional stress, fatigue and fracture strength in silicon hinges of a micro scanning mirror," 2004, pp. 176-185.

[41] J. Il Woong, S. Kim, and O. Solgaard, "High-Reflectivity Broadband Photonic Crystal Mirror MEMS Scanner With Low Dependence on Incident Angle and Polarization," *Microelectromechanical Systems, Journal of,* vol. 18, pp. 924-932, 2009.

[42] B. Le Foulgoc, A. Bosseboeuf, T. Bourouina, O. Le Traon, S. Masson, and A. Parent, "An Experimental Study of Nonlinear Limits in High-Q Silicon Vibrating Micro-and Nanomechanical Sensors," in *Solid-State Sensors, Actuators and Microsystems Conference, 2007. TRANSDUCERS 2007. International*, 2007, pp. 1721-1724.

[43] C. Hoy, N. Durr, C. Pengyuan, D. K. Smith, T. Larson, W. Piyawattanametha, R. Hyejun, B. Korgel, K. Sokolov, O. Solgaard, and A. Ben-Yakar, "Two-photon luminescence imaging using a MEMS-based miniaturized probe," in *Lasers and Electro-Optics, 2008 and 2008 Conference on Quantum Electronics and Laser Science. CLEO/QELS 2008. Conference on*, 2008, pp. 1-2.

[44] A. D. Yalcinkaya, O. Ergeneman, and H. Urey, "Polymer magnetic scanners for barcode applications," *Sensors and Actuators A: Physical,* vol. 135, pp. 236-243, 2007.

[45] J. Kim and L. Lin, "Electrostatic scanning micromirrors using localized plastic deformation of silicon," *Journal of Micromechanics and Microengineering,* vol. 15, p. 1777, 2005.

[46] M. Yoda, K. Isamoto, C. Chong, H. Ito, A. Murata, and H. Toshiyoshi, "Design and fabrication of a MEMS 1-D optical scanner using self-assembled vertical combs and scan-angle magnifying mechanism," in *Optical MEMS and Their Applications Conference, 2005. IEEE/LEOS International Conference on*, 2005, pp. 19-20.

[47] S. Kurth, C. Kaufmann, R. Hahn, J. Mehner, W. Doetzel, and T. Gessner, "A novel 24-kHz resonant scanner for high-resolution laser display," San Jose, CA, USA, 2005, pp. 23-33.

[48] J. Chang-Hyeon, K. Seong-Hyok, Y. Youngjoo, C. Moongoo, K. Sang-Cheon, L. See-Hyung, and B. Jong-Uk, "Diamond shaped frame supported electrostatic scanning micromirror," in *Solid-State Sensors, Actuators and Microsystems, 2005. Digest of Technical Papers. TRANSDUCERS '05. The 13th International Conference on*, 2005, pp. 992-995 Vol. 1.

[49] H. Schenk, P. Durr, T. Haase, D. Kunze, U. Sobe, H. Lakner, and H. Kuck, "Large deflection micromechanical scanning mirrors for linear scans and pattern generation," *Selected Topics in Quantum Electronics, IEEE Journal of*, vol. 6, pp. 715-722, 2000.

[50] A. Arslan, S. Holmstrom, S. K. Gokce, and H. Urey, "Comb- Actuated resonant torsional scanner for microdisplays," in *Optical MEMS and Nanophotonics, 2009 IEEE/LEOS International Conference on*, 2009, pp. 139-140.

[51] T. Sandner, T. Klose, A. Wolter, H. Schenk, H. K. Lakner, and W. Davis, "Damping analysis and measurement for a comb-drive scanning mirror," Strasbourg, France, 2004, pp. 147-158.

[52] A. D. Yalcinkaya, H. Urey, D. Brown, T. Montague, and R. Sprague, "Two-axis electromagnetic microscanner for high resolution displays," *Microelectromechanical Systems, Journal of*, vol. 15, pp. 786-794, 2006.

[53] D. W. Wine, M. P. Helsel, L. Jenkins, H. Urey, and T. D. Osborn, "Performance of a biaxial MEMS-based scanner for microdisplay applications," 2000, pp. 186-196.

[54] S. Hsu, T. Klose, C. Drabe, and H. Schenk, "Fabrication and characterization of a dynamically flat high resolution micro-scanner," *Journal of Optics a-Pure and Applied Optics*, vol. 10, pp. -, Apr 2008.

[55] J. H. Park, J. Akedo, and H. Sato, "High-speed metal-based optical microscanners using stainless-steel substrate and piezoelectric thick films prepared by aerosol deposition method," *Sensors and Actuators a-Physical*, vol. 135, pp. 86-91, Mar 30 2007.

[56] M. C. H. Ji, S. C. Kim, S. H. Lee, S. H. Kim, Y. Yee, and J. U. Bu, "An electrostatic scanning micromirror with diaphragm mirror plate and diamond-shaped reinforcement frame," *Journal of Micromechanics and Microengineering*, vol. 16, p. 1033, 2006.

[57] V. Milanovic, G. A. Matus, and D. T. McCormick, "Gimbal-less monolithic silicon actuators for tip-tilt-piston micromirror applications," *Selected Topics in Quantum Electronics, IEEE Journal of*, vol. 10, pp. 462-471, 2004.

[58] J.-W. Cho, Y.-H. Park, Y.-C. Ko, B.-L. Lee, S.-J. Kang, S.-W. Chung, W.-k. Choi, Y.-C. Cho, S.-M. Chang, J.-H. Lee, and J. Sunu, "Electrostatic 1D microscanner

with vertical combs for HD resolution display," San Jose, CA, USA, 2007, pp. 64660B-12.

[59] A. A. Kuijpers, D. Lierop, R. H. M. Sanders, J. Tangenberg, H. Moddejonge, J. W. T. Eikenbroek, T. S. J. Lammerink, and R. W. Wiegerink, "Towards embedded control for resonant scanning MEMS micromirror," *Procedia Chemistry,* vol. 1, pp. 1307-1310, 2009.

[60] T. T. Torashima K. , Mizoguchi Y. , Yasuda S. , Kato T. , Shimada Y. and Yagi T. , "A micro scanner with low power consumption using double coil layers on a permalloy film," in *IEEE-LEOS Conf. Optical MEMS 2004*, 2004.

[61] Y. C. Ko, J. W. Cho, Y. K. Mun, H. G. Jeong, W. K. Choi, J. W. Kim, Y. H. Park, J. B. Yoo, and J. H. Lee, "Eye-type scanning mirror with dual vertical combs for laser display," *Sensors and Actuators a-Physical,* vol. 126, pp. 218-226, Jan 26 2006.

VITA

Sertan Kutal Gökçe was born in Adana, Turkey in 1985. He received the B.Sc. degree in Electrical and Electronics engineering from Middle East Technical University, Ankara, Turkey in 2008. During his undergraduate studies, he was in Drexel University, Philadelphia, PA as a summer intern. He is currently working toward the M.Sc.degree at Koç University, Istanbul, Turkey, with Hakan Ürey. He was in EPFL, Lausanne, Switzerland from (02/2009–09/2009) as an exchange research scholar to use cleanroom facilities. His current research focus is FEM design and microfabrication of MEMS-based scanners. His research interests are microsystems and MEMS structures for biological and optical applications. He is a student member of IEEE and IEEE-LEOS.